Chemical Rate Theory and Radiation Damage Modeling

Using IM3D Output and Python Code

Dr. Muhammad Saadat Shakoor KHAN
Hefei Institute of Physical Sciences,
Chinese Academy of Sciences

Supervised By:

Prof. Yonggang Li
Institute of Solid State Physics,
Chinese Academy of Sciences

Version: 1.0
November 12, 2025

Contents

Chapter 1

Introduction

1.1 Fundamentals of Radiation Damage

When energetic particles (such as neutrons, ions, or electrons) strike a solid, they can knock atoms out of their lattice sites. The first atom displaced by an incident particle is called the **primary knock-on atom (PKA)**. If the PKA has enough kinetic energy (exceeding the threshold displacement energy E_d of the material), it can leave its lattice site and collide with neighboring atoms. Each such collision can transfer energy to another atom; if that atom receives energy $> E_d$, it too is displaced. This sequence of collisions produces a **collision cascade** of atomic displacements.

Each atom permanently displaced from the lattice creates a pair of defects: a vacant lattice site (**vacancy**) and the knocked-out atom now trapped in the lattice somewhere between regular sites (an **interstitial**). This vacancy–interstitial pair is known as a **Frenkel pair**, the fundamental product of radiation damage in a crystal. A single energetic PKA can generate many Frenkel pairs in a localized region (on the order of nanometers), depending on its energy. Lower energy radiation may produce only a few point defects (or none if the energy is below E_d), whereas higher energy radiation yields cascades with a larger number of point defects.

To quantify radiation damage, the concept of **displacements per atom (dpa)** is used. 1 dpa means that on average each atom in the material has been displaced once from its site. It is essentially a normalized measure of the number of lattice displacements. For example, 0.1 dpa indicates that 10% of atoms have been displaced on average. The total number of atomic displacements (and thus the dpa) produced by an irradiation

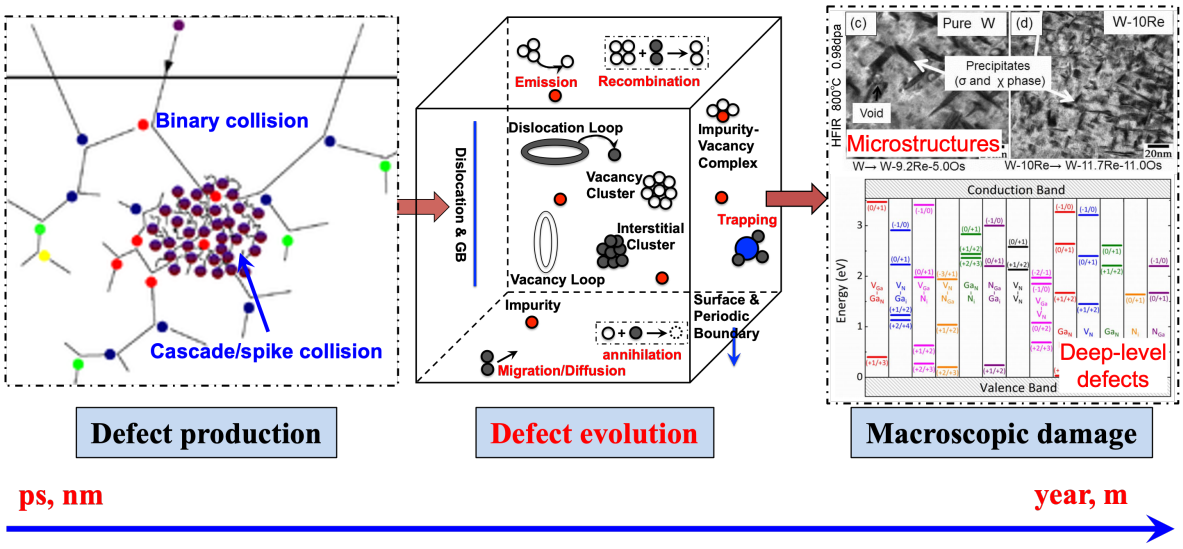

Figure 1.1: Schematic of a collision cascade in a crystalline solid. An incoming particle creates a PKA which displaces lattice atoms, resulting in vacancies (open circles) and interstitials (filled circles) along its path. (Placeholder figure)

depends on the energy and flux of incoming particles and the material's properties (such as E_d).

The number of defects produced by a single PKA of damage energy E_a can be estimated by the Kinchin-Pease model (as modified by Norgett, Robinson and Torrens). For high PKA energies ($E_a \gg E_d$), the model predicts approximately:

$$N_{\mathrm{FP}}(E_a) \;\approx\; 0.8\,\frac{E_a}{2\,E_d}\;, \tag{1.1}$$

where N_{FP} is the number of Frenkel pairs (i.e. vacancies or interstitials) created. This relation implies that roughly one Frenkel pair is produced per $2E_d$ of available energy (with an efficiency factor of 0.8 from empirical adjustment). For E_a just above the threshold E_d, typically one Frenkel pair is created (the PKA itself becomes an interstitial and leaves behind one vacancy). If E_a is below E_d, no permanent damage occurs. The displacements per atom can be calculated by summing the contributions of many such PKAs over the irradiation dose. In practice, standards for calculating dpa (e.g. the NRT formula above) are used to estimate damage rates under neutron or ion irradiation.

After the initial cascade, the population of defects can evolve through diffusion and interactions. Vacancies and interstitials might recombine (annihilating each other) or aggregate into larger defect structures (such as vacancy clusters/voids or interstitial clusters forming dislocation loops) especially if the material is at an elevated temperature.

These processes, along with continuous defect production under irradiation, determine the long-term **radiation damage evolution** in the material. To model and predict this evolution, several approaches are utilized in radiation damage studies: **Binary-collision Monte Carlo simulations**: Tools like SRIM or specialized Monte Carlo codes simulate the collision cascade by treating atom–atom collisions statistically. They predict the initial spatial distribution of defects and the total defect count (dpa) from a given irradiation condition. **Molecular Dynamics (MD) simulations**: MD directly simulates the motion of atoms during a cascade. It can capture detailed cascade morphology and defect structures, and accounts for dynamic interactions and rapid recombination within the cascade. MD is useful for validating the defect production efficiency (e.g. the factor 0.8 above) and understanding defect clustering in cascades. **Rate theory (chemical rate theory)** and **cluster dynamics**: These are continuum modeling approaches used to simulate the time evolution of defect concentrations under ongoing irradiation. Rate theory sets up differential equations for point defect populations and their sinks (e.g. grain boundaries, dislocations) — including terms for defect generation (source term proportional to the irradiation rate), recombination of interstitials and vacancies, and absorption of defects at sinks. By solving these rate equations, one can predict how the concentrations of vacancies, interstitials, and larger defect clusters change with dose, temperature, and time. Cluster dynamics extends this to track size distributions of clusters (voids, loops) explicitly. **Kinetic Monte Carlo (KMC)**: An atomistic simulation technique that evolves the system through random events (like defect migration, recombination events) with proper kinetics. KMC can model long-term microstructural changes caused by radiation (such as growth of voids or precipitates) over timescales that are inaccessible to direct MD simulations.

Each modeling method has its role: Monte Carlo and MD deal with the *primary damage state* (fast processes during and immediately after a cascade, up to picoseconds), whereas rate theory, cluster dynamics, and KMC address *post-cascade evolution* (slower processes over seconds to years). By combining these tools, researchers can bridge the scales from atomistic defect production to macroscopic material property changes. In summary, the fundamentals of radiation damage involve understanding how energetic particles produce point defects in materials and using appropriate models to describe the creation and evolution of these defects over time, which is crucial for predicting material

performance in radiation environments.

1.2 Why Use Computational Models in Radiation Damage Studies

Experimental studies are invaluable for understanding radiation damage in materials, but they have significant practical limitations. In many cases, it is not feasible to capture all the relevant phenomena through experiments alone. Some key limitations include:

- **Access to atomic-scale details:** Radiation damage processes occur at the atomic scale and on extremely short timescales (picoseconds to microseconds), which are nearly impossible to observe directly with current experimental techniques. Instruments like high-speed cameras or *in situ* microscopes cannot fully capture individual atomic collisions and defect formations in real time.
- **Time and dose constraints:** Reproducing long-term irradiation effects in the lab is often impractical. Materials in a reactor core experience years of neutron or ion irradiation; performing an equivalent experiment would be time-prohibitive. Accelerated irradiation (using higher particle flux) can shorten test duration, but it may not faithfully replicate the gradual damage accumulation that occurs over decades of service.
- **Cost and safety:** High-dose irradiation experiments require specialized facilities (such as nuclear reactors or particle accelerators) and can be extremely expensive. They also produce radioactive samples, making handling and post-irradiation analysis challenging and hazardous. These factors limit the number and scope of experiments that can be conducted.
- **Limited diagnostic insight:** Even when irradiation experiments are performed, measurements often give only bulk or post-mortem information (for example, an increase in hardness or the amount of swelling after irradiation). Such results alone do not reveal the underlying atomic-scale mechanisms—how individual defects migrate, interact, and cluster to produce the observed property changes.

Computational modeling helps bridge this gap by simulating radiation damage in a controlled virtual environment. Using simulations, researchers can observe the detailed behavior of atoms and defects during and after irradiation, and explore "what-if" scenarios

(varying radiation doses, energies, temperatures, etc.) that would be difficult to test experimentally. Moreover, computational models allow us to study radiation effects across multiple length and time scales, from atomic-level events up to macroscopic material behavior. In radiation damage studies, several computational methods are commonly used, each addressing different scales and aspects of the problem:

- **Molecular Dynamics (MD):** MD uses physics-based interatomic potentials to simulate the motions of atoms. It is well-suited for studying the immediate aftermath of an energetic particle impact, known as a collision cascade. For example, MD can model a primary knock-on atom (PKA) striking a lattice and causing a cascade of atomic displacements, resulting in the creation of point defects (vacancies and interstitials) and defect clusters. These simulations provide atomic-level insight into damage formation and defect configurations within the first few picoseconds or nanoseconds of irradiation. However, because MD explicitly calculates every atomic interaction in small time increments (femtoseconds), it is limited to short physical times and relatively small simulation volumes. This means MD cannot directly simulate long-term evolution of radiation damage (like many seconds, hours, or beyond) or the behavior of a bulk component over its entire service life.
- **Monte Carlo simulations (e.g., *IM3D*):** Monte Carlo methods use random sampling to simulate processes in a probabilistic manner. In radiation damage contexts, Monte Carlo codes like *IM3D* efficiently model the effect of energetic particles on a material by statistically tracking their interactions. For example, a binary collision approximation (BCA) Monte Carlo algorithm will follow a high-energy PKA through the material, randomly sampling collision events based on known physics to predict how many defects are produced, what types they are, and how far they are distributed from the impact point. By treating collisions and reactions statistically rather than tracking every atom's motion, Monte Carlo simulations can cover larger spatial volumes or simulate many repeated irradiation events more feasibly than MD. This approach is useful for bridging from the atomistic scale to higher scales, handling radiation effects on intermediate length scales and timescales. For instance, one can use Monte Carlo results to estimate the immediate defect density after a large number of cascade events, which serves as input for higher-level models.

- **Rate Theory (CRT):** Rate theory is a continuum approach (often referred to as reaction-rate theory or cluster dynamics) that describes the evolution of defect populations with time using average concentrations. Instead of dealing with individual atoms, CRT models treat defects (like vacancies, interstitials, and their clusters) as variables in a set of coupled differential equations. These equations represent processes such as defect generation by irradiation, recombination of interstitials and vacancies (mutual annihilation), migration of defects to sinks (like grain boundaries or dislocations), and clustering into larger defect structures. By solving these rate equations, one can predict how the concentrations of various defects change over extended periods under steady irradiation conditions. Because this method is not limited by small time-step calculations, it can easily span very long timescales — from seconds to hours, and even to years of equivalent radiation exposure. In other words, CRT enables researchers to extrapolate and predict long-term radiation effects (for example, the growth of voids leading to swelling, or the accumulation of helium in bubbles, or overall embrittlement trends) over the lifetime of a component. This capability to reach reactor-relevant timescales is the primary reason why rate theory is used for long-term predictions: it fills the gap that neither MD nor direct Monte Carlo simulations can cover. The accuracy of CRT depends on inputs (diffusion coefficients, reaction rates, etc.) often obtained from experiments or lower-scale simulations, but when calibrated, it becomes a powerful tool to forecast material behavior under prolonged irradiation.

In practice, these computational methods are complementary, and a *multiscale modeling* strategy can integrate them to achieve more comprehensive predictions. For instance, MD simulations provide quantitative data on defect formation energies and migration barriers, which can feed into Monte Carlo or rate theory models. Monte Carlo simulations (like IM3D or kinetic Monte Carlo variants) can simulate the accumulation and spatial distribution of damage over many cascades or diffusion events, bridging the gap toward higher defect densities. Finally, rate theory can take the output of these methods (such as initial defect densities and reaction rates) to project the material's evolution over long times under continuous irradiation. By combining insights from all these modeling approaches with targeted experiments for validation, researchers can attain a much deeper understanding of radiation damage mechanisms. This combined approach allows us to

predict material performance in regimes that are impractical to fully test experimentally, thereby guiding the design and selection of more radiation-tolerant materials.

Chapter 2

Chemical Rate Theory (CRT)

2.1 Introduction to CRT

Chemical Rate Theory (CRT) is a powerful framework used to model the evolution of radiation-induced point defects in materials under irradiation [19, 23]. It describes the population of defects such as vacancies and interstitials over time by solving coupled ordinary differential equations (ODEs).

CRT assumes that defects are:

- Uniformly distributed (no spatial variation),
- Governed by generation, recombination, and absorption at sinks,
- Mostly single-point defects (clusters can be included but increase model complexity).

It is widely used because it captures the **average behavior** of defect dynamics without needing full atomistic simulations [18, 4].

2.2 Governing Equations

The evolution of vacancy concentration $C_V(t)$ and interstitial concentration $C_I(t)$ can be described by the following ODEs [18, 23]:

$$\frac{dC_V}{dt} = G - R\,C_V\,C_I - K_{\text{sink}}\,D_V\,C_V, \tag{2.1}$$

$$\frac{dC_I}{dt} = G - R\,C_V\,C_I - K_{\text{sink}}\,D_I\,C_I. \tag{2.2}$$

Where:

- G: Defect generation rate (displacements per atom per second, dpa/s),
- R: Recombination rate coefficient (m^3/s),
- K_{sink}: Sink strength (m^{-2}),
- D_V, D_I: Diffusion coefficients of vacancies and interstitials (m^2/s).

2.3 Physical Meaning of Each Term

- **Generation Term (G)**: New Frenkel pairs (vacancy + interstitial) created by irradiation [15].
- **Recombination Term ($R\,C_V\,C_I$)**: Vacancies and interstitials recombine, annihilating each other [19].
- **Sink Terms ($K_{\text{sink}}\,D\,C$)**: Defects are absorbed at microstructural sinks such as grain boundaries or dislocations [18, 24].

2.4 Expressions for Key Parameters

- Diffusion coefficients follow Arrhenius relations [4, 23]:

$$D = D_0 \exp\left(-\frac{E_m}{k_B T}\right) \tag{2.3}$$

  where:
  - D_0: Diffusion prefactor (m^2/s),
  - E_m: Migration energy (eV),
  - k_B: Boltzmann constant (8.617×10^{-5} eV/K),
  - T: Temperature (K).

- Recombination rate coefficient [18]:

$$R = \frac{4\pi(D_V + D_I)}{a^2} \tag{2.4}$$

  where a is the lattice constant (m).

- Sink strength approximation for grain boundaries [23]:

$$K_{\text{sink}} = \frac{57.6}{d^2} \tag{2.5}$$

  where d is grain size (m).

2.5 Steady-State Solution

At long irradiation times, a steady-state is reached where:

$$\frac{dC_V}{dt} = \frac{dC_I}{dt} = 0. \tag{2.6}$$

This condition yields [18, 19]:

$$G = R\,C_V\,C_I + K_{\text{sink}}\,D_V\,C_V, \tag{2.7}$$

$$G = R\,C_V\,C_I + K_{\text{sink}}\,D_I\,C_I. \tag{2.8}$$

Solving these equations together gives steady-state concentrations C_V and C_I.

At steady-state, a key relationship is:

$$D_V\,C_V = D_I\,C_I, \tag{2.9}$$

indicating balanced fluxes of vacancies and interstitials to sinks.

2.6 When and Why Use CRT

Chemical Rate Theory (CRT) is particularly suitable for simulating long-term microstructural evolution under irradiation [19, 4, 23, 14]. It excels when:

- Simulating defect accumulation and recombination over long timescales (seconds to hours),
- Capturing averaged defect behavior where atomistic resolution is unnecessary or computationally prohibitive,
- Modeling the influence of grain boundaries, interfaces, and sinks in nanocrystalline or superlattice materials,
- Evaluating the impact of macroscopic variables such as grain size, irradiation dose rate, and temperature,
- Efficient computation is prioritized for parametric or sensitivity analyses.

CRT is especially effective for **nanocrystalline metals**, **oxide-dispersion-strengthened alloys**, and **superlattice structures**, where high interface densities dominate defect kinetics and sink strengths. In such cases, molecular dynamics (MD) or kinetic Monte Carlo (KMC) simulations become infeasible due to time or length scale limitations [14, 23].

2.7 When and Why Use KMC

Kinetic Monte Carlo (KMC) is well-suited for capturing spatially resolved, stochastic behavior of defect evolution, particularly when:

- Modeling specific defect migration paths or event-driven diffusion,
- Tracking individual defects, clusters, or solutes over short to medium timescales (microseconds to seconds),
- Exploring spatial correlations in defect-defect or defect-interface interactions,
- Studying anisotropic diffusion, trapping, or segregation at interfaces,
- Fine-tuned calibration with experimental data is available.

As noted in Zheng et al. [23], KMC enables realistic simulation of 3D defect dynamics in precipitate-rich alloys. It has been successfully used to model early-stage defect absorption at coherent precipitate interfaces and competitive diffusion near grain boundaries [14]. However, KMC becomes limited when:

- Simulation spans long timescales (hours or more),
- Large system sizes (hundreds of nm) are required,
- Defect-sink interaction statistics can be averaged.

2.8 Comparison Between CRT, MD, and KMC

As shown in the Table 2.2, CRT is ideal for fast parametric simulations over engineering-relevant timescales, especially for superlattice and nanocrystalline systems. KMC fills the gap when spatial and statistical accuracy is needed, and MD is essential for validating initial defect generation mechanisms (e.g., via iM3D or SRIM) [14].

Table 2.1: Comparison of radiation damage modeling techniques

Aspect	**CRT**	**KMC**	**MD**
Time scale	Continuous (years)	1 µs to 100 µs — 1 s to 10 s	Femtoseconds–nanoseconds
Length scale	[a]Millimeter scale	Nanoparticle assemblies (1 nm–100 µm)	Atomic-level trajectories (<1 nm)
Computational cost	Low (hours/days)	Medium (days/weeks)	High (weeks/months)
Physical approach	Cluster rate equations	Discrete defect jumping	First-principles forces
Key strength	• Dose-dependence prediction • Analytic solutions	• Microstructure evolution • Sink strength analysis	• Primary knock-on events • Threshold displacement
Weakness	No spatial correlation	Ignored elastic interactions	Ionization effects omitted

Typical application ranges shown [4, 23, 14]

Chapter 3

Detailed Code Explanation and Link to CRT Theory

This Python script implements the chemical rate Theory (CRT) discussed in Chapter 1. Each part of the code directly corresponds to the mathematical equations previously introduced.

3.1 User Inputs

At the beginning, the user is prompted to input three fundamental parameters:

- **Generation rate G (dpa/s)**: Controls how many Frenkel pairs are produced per second per atom. Corresponds to the source term in Equations (2.1) and (2.2).
- **Temperature T (K)**: Affects defect mobilities through diffusion coefficients (Equation (2.3)).
- **Grain size d (m)**: Determines the sink strength (Equation (2.5)).

3.2 Physical Constants and Material Properties

Physical constants like Boltzmann constant k_B and lattice constant a are defined.

Diffusion prefactors D_0 and migration energies E_m are specified for:

- Vacancies (D_{0V}, E_{mV}),
- Interstitials (D_{0I}, E_{mI}).

These values are used in the Arrhenius equation for calculating diffusivities.

3.3 Diffusion Coefficient Calculation

Using the Arrhenius relation (Equation (1.4)):

$$D = D_0 \exp\left(-\frac{E_m}{k_B T}\right),$$

the temperature-dependent diffusivities D_V and D_I are computed.

These coefficients represent how quickly vacancies and interstitials move through the lattice.

3.4 Recombination Rate and Sink Strength

- The recombination coefficient R is calculated by:

$$R = \frac{4\pi(D_I + D_V)}{a^2},$$

  describing how efficiently vacancies and interstitials annihilate each other.

- The sink strength K_{sink} is determined by:

$$K_{\text{sink}} = \frac{57.6}{d^2},$$

  modeling the effect of grain boundaries and other sinks.

3.5 Setting up the ODE System

The heart of CRT is solving the two coupled rate equations:

$$\frac{dC_V}{dt} = G - R\,C_V\,C_I - K_{\text{sink}}\,D_V\,C_V \quad \text{(Equation (2.1))},$$

$$\frac{dC_I}{dt} = G - R\,C_V\,C_I - K_{\text{sink}}\,D_I\,C_I \quad \text{(Equation (2.2))}.$$

These equations govern the evolution of the concentrations of vacancies $C_V(t)$ and interstitials $C_I(t)$.

In the code, the function `defect_evolution` directly implements these equations.

3.6 Initial Conditions

We assume no pre-existing radiation damage, setting:

$$C_V(0) = 0, \quad C_I(0) = 0.$$

Thus, all defects generated during simulation come from irradiation.

3.7 ODE Solution Strategy

The solver `solve_ivp` from `scipy.integrate` is used with:

- Method = `Radau` (suitable for stiff systems),
- Time span = $[0, t_{\text{end}}]$,
- Dense output for interpolation.

We solve for $C_V(t)$ and $C_I(t)$ over time.

The stiffness arises because $C_I(t)$ can equilibrate very rapidly compared to $C_V(t)$.

3.8 Simulation Implementation and Input Parameters

3.8.1 Overview

This Python-based chemical rate theory (CRT) simulation code is designed to model the evolution of Fe–Ni–Al nanoparticle precipitates embedded in a body-centered cubic (bcc) Fe matrix. Its purpose is to simulate the time-dependent behavior of precipitate cluster populations, providing insight into the nucleation, growth, and coarsening kinetics of Ni–Al clusters under specified conditions. The code implements the theoretical

framework described in Chapter2 by solving the governing system of ordinary differential equations (ODEs) for cluster population dynamics (see Chapter2, Eq. (2.1) and related equations), without repeating those equations here. In doing so, it bridges the theory to a computational tool that can predict microstructural evolution over time. For clarity and modularity, the implementation is divided into four major components:

- **Input handling:** Reads and processes user-defined input parameters (e.g., alloy composition, temperature, initial solute content, cluster size range, and simulation time settings). This stage establishes the initial conditions of the simulation, ensuring the code is configured with the correct material properties and starting cluster distribution.
- **Parameter setup:** Initializes all necessary physical and model parameters required by the CRT equations. This includes quantities such as diffusion coefficients, cluster formation energies, reaction rate constants, and other material-specific constants, which are drawn from the theory in Chapter2 or relevant literature. By setting these parameters, the code defines the rates of processes like atomic diffusion and cluster reactions in accordance with the CRT model.
- **Differential equation solver:** Uses a numerical ODE solver to integrate the cluster population rate equations over the simulated time span. This is the core of the simulation, where the code computes the evolution of cluster number densities for each cluster size. A suitable integration scheme (capable of handling stiff equations, if necessary) ensures stable and accurate solution of the coupled ODEs that govern nucleation, growth, and dissolution of clusters.
- **Post-processing:** Analyzes the output of the solver and produces meaningful results for the user. This stage computes key outcomes such as the precipitate number density, volume fraction, and average cluster size as functions of time. It can also generate tables, figures, or plots to visualize the cluster size distribution evolution. Such post-processing helps interpret the simulation results in the context of the theoretical expectations from Chapter2 and can facilitate comparison with experimental data.

```
1 ##################################################
2 #  Module Name : crt-np
3 #  Module Date : 04/15/2025
4 #  Module Auth : Yonggang Li, ygli@theory.issp.ac.cn, ISSP, CAS
```

```
#
#  Description : A rate theory model used to solve the radiation damage of
#                nanoparticle superlattice systems in steady or unsteady states.
##################################################

import tkinter as tk  # GUI library
from tkinter import messagebox, filedialog
import numpy as np  # Numerical arrays
from scipy.integrate import solve_ivp  # ODE solver
import matplotlib.pyplot as plt  # Plotting
import time  # Time measurement

k_B = 8.617e-5  # Boltzmann constant (eV/K)

# Function to save simulation results to file
def save_data_to_file(time_data, CI_data_p, CV_data_p, CI_data_b, CV_data_b, filename="./C-I-V-t.dat"):
    try:
        data = np.column_stack((time_data, CI_data_p, CV_data_p, CI_data_b, CV_data_b))
        header = "Time (s)    SIA Concentration (dpa)    Vacancy Concentration (dpa)"
        np.savetxt(filename, data, header=header, comments="", fmt='%.6e')
    except Exception as e:
        messagebox.showerror("Error", f"An error occurred while saving data: {str(e)}")

# Main simulation function
def run_simulation():
    try:
        start_time = time.time()

        # GUI input retrieval
        T = float(entry_T.get())
        tmax = float(entry_tmax.get())

```

```
        G_p = float(entry_G_p.get())
        EmI_p = float(entry_EmI_p.get())
        D0I_p = float(entry_D0I_p.get())
        EfI_p = float(entry_EfI_p.get())
        EmV_p = float(entry_EmV_p.get())
        D0V_p = float(entry_D0V_p.get())
        EfV_p = float(entry_EfV_p.get())
        d_p = float(entry_d_p.get())
        pv_p = float(entry_pv_p.get())
        a_p = float(entry_a_p.get())

        Vatom_p = a_p ** 3 / 2
        G_p /= Vatom_p

        G_b = float(entry_G_b.get())
        EmI_b = float(entry_EmI_b.get())
        D0I_b = float(entry_D0I_b.get())
        EfI_b = float(entry_EfI_b.get())
        EmV_b = float(entry_EmV_b.get())
        D0V_b = float(entry_D0V_b.get())
        EfV_b = float(entry_EfV_b.get())
        d_b = float(entry_d_b.get())
        a_b = float(entry_a_b.get())

        d_b = ((1 - pv_p) / pv_p) ** (1 / 3) * d_p
        Vatom_b = a_b ** 3 / 2
        G_b /= Vatom_b

        if T < 1 or T > 3000:
            raise ValueError("Temperature out of valid range (1  3000
               K)")
        if d_p < 1e-9:
            raise ValueError("Particle size must be >= 1e-9 m")

        def rate_coefficient(D0I, EmI, D0V, EmV, a, d):
            DI = D0I * np.exp(-EmI / (k_B * T))
            DV = D0V * np.exp(-EmV / (k_B * T))
            kr = 4 * np.pi * (DI + DV) / a ** 2
            ksI = 57.6 / d ** 2
```

```
            return DI, DV, kr, ksI

        DI_p, DV_p, kr_p, ksI_p = rate_coefficient(D0I_p, EmI_p, D0V_p,
            EmV_p, a_p, d_p)
        ksV_p = ksI_p
        DI_b, DV_b, kr_b, ksI_b = rate_coefficient(D0I_b, EmI_b, D0V_b,
            EmV_b, a_b, d_b)
        ksV_b = ksI_b

        def solver(flag):
            t_span = (1e-13, tmax)
            num_points = 100
            t_eval = np.logspace(np.log10(t_span[0]), np.log10(t_span
                [1]), num_points)

            if flag == 0:
                G, kr, Vatom, ksI, ksV, DI, DV, EfI, EfV = G_p, kr_p,
                    Vatom_p, ksI_p, ksV_p, DI_p, DV_p, EfI_p, EfV_p
            else:
                G, kr, Vatom, ksI, ksV, DI, DV, EfI, EfV = G_b, kr_b,
                    Vatom_b, ksI_b, ksV_b, DI_b, DV_b, EfI_b, EfV_b

            y0 = [np.exp(-EfI / (k_B * T)) / Vatom, np.exp(-EfV / (k_B
                * T)) / Vatom]

            def defect_evolution(t, y):
                CI, CV = y
                dCI_dt = G - kr * CI * CV * Vatom - ksI * DI * CI
                dCV_dt = G - kr * CI * CV * Vatom - ksV * DV * CV
                return [dCI_dt, dCV_dt]

            sol = solve_ivp(defect_evolution, t_span, y0, t_eval=t_eval
                , method='LSODA')
            CI, CV = sol.y * Vatom
            CI_max = np.max(CI)
            CV_max = np.max(CV)
            tol = 0.1 * CV_max
            steady_index = next((i for i in range(len(CV)) if abs(CV[i]
                - CV_max) < tol), -1)
```

```
106             steady_time = sol.t[steady_index] if steady_index != -1
                    else 'N/A'
107             return sol.t, CI, CV, CI_max, CV_max, steady_time
108
109         time_p, CI_p, CV_p, CI_max_p, CV_max_p, steady_time_p = solver
                (0)
110         time_b, CI_b, CV_b, CI_max_b, CV_max_b, steady_time_b = solver
                (1)
111         save_data_to_file(time_p, CI_p, CV_p, CI_b, CV_b)
112
113         plt.figure()
114         plt.plot(time_p, CI_p, label='SIA (I) - p')
115         plt.plot(time_p, CV_p, label='Vacancy (V) - p')
116         plt.plot(time_b, CI_b, label='SIA (I) - b')
117         plt.plot(time_b, CV_b, label='Vacancy (V) - b')
118         plt.xscale('log')
119         plt.yscale('log')
120         plt.xlabel('Time (s)')
121         plt.ylabel('Concentration (dpa)')
122         plt.title(f"T={T}K, d_p={d_p*1e9:.1f}nm, d_b={d_b*1e9:.1f}nm")
123         plt.legend()
124         plt.grid(True, which="both", ls="--")
125         plt.tight_layout()
126         plt.show()
127
128     except Exception as e:
129         messagebox.showerror("Error", str(e))
130
131 def save_figure():
132     filename = filedialog.asksaveasfilename(defaultextension=".png")
133     if filename:
134         plt.savefig(filename)
135         messagebox.showinfo("Success", f"Figure saved to {filename}")
136
137 # GUI setup
138 root = tk.Tk()
139 root.title("Point Defect Evolution Simulation with Interface Absorption
    ")
140
```

```
params = {
    "Temperature T (K)": "300",
    "Maximum time t_max (s)": "1e3",
    "Generation Rate G_p (dpa/s)": "1e-6",
    "Migration Energy of I_p (eV)": "0.013",
    "Pre-factor D0^I_p (m  /s)": "1e-8",
    "Formation Energy of I_p (eV)": "9.466",
    "Migration Energy of V_p (eV)": "1.66",
    "Pre-factor D0^V_p (m  /s)": "1e-6",
    "Formation Energy of V_p (eV)": "3.8",
    "Particle/Grain Size d_p (m)": "1e-6",
    "Percentage of particle volume": "0.1",
    "Lattice constant a_p (m)": "3.165e-10",
    "Generation Rate G_b (dpa/s)": "1e-4",
    "Migration Energy of I_b (eV)": "0.14",
    "Pre-factor D0^I_b (m  /s)": "4.55e-2",
    "Formation Energy of I_b (eV)": "4.5",
    "Migration Energy of V_b (eV)": "1.6",
    "Pre-factor D0^V_b (m  /s)": "2.5e-5",
    "Formation Energy of V_b (eV)": "1.79",
    "Particle/Grain Size d_b (m)": "4e-8",
    "Lattice constant a_b (m)": "3.52e-10",
}

entries = {}
for i, (label, default) in enumerate(params.items()):
    tk.Label(root, text=label).grid(row=i, column=0, sticky='e')
    entry = tk.Entry(root)
    entry.insert(0, default)
    entry.grid(row=i, column=1)
    entries[label] = entry

entry_T = entries["Temperature T (K)"]
entry_tmax = entries["Maximum time t_max (s)"]

tk.Button(root, text="Run Simulation", command=run_simulation).grid(row
    =len(params), column=0, pady=10)
tk.Button(root, text="Save Plot", command=save_figure).grid(row=len(
    params), column=1)
```

```
178
179 root.mainloop()
```

Listing 3.1: CRT-NP Python simulation script with GUI

3.9 Input Parameters

This section outlines the input parameters for **BCC Fe bulk** and **Fe-Ni-Al alloy precipitates**, derived from experimental and computational studies.

3.9.1 Defect Properties of Fe-Ni-Al Alloy Precipitates and BCC Fe

3.9.2 Parameter Justification and Calculation Methodology

The defect properties presented in Table 3.1 were selected through careful consideration of both experimental measurements and theoretical calculations. This section details the rationale behind parameter selection and the computational methodology employed.

Selection of Reported Values

Reported values were chosen based on the following criteria:

- **BCC Fe bulk properties** were taken from established experimental studies [10, 7] and large-scale molecular dynamics simulations [3], as these provide the most reliable reference data for pure iron systems.
- **Fe-Ni-Al precipitate values** were selected from:
  - Ni_3Al studies [21, 11] for vacancy-related properties
  - Fe-Ni system investigations [8, 1] for migration barriers
  - Radiation damage studies [12, 16] for interstitial properties
- When multiple sources reported different values, we adopted:

$$\bar{X} = \frac{1}{N}\sum_{i=1}^{N} X_i \pm \sigma \tag{3.1}$$

where $\bar{X}$ is the mean value and σ the standard deviation across studies.

Table 3.1: Defect properties for **Fe-Ni-Al alloy** precipitates and **BCC Fe bulk**, including reported and LAMMPS-calculated values.

Defect Property	**Reported Values**	**LAMMPS**	**Unit**	**Source**
BCC Fe (Bulk)				
Vacancy Formation Energy	1.1 eV		eV	[10]
Vacancy Migration Energy	0.7–1.0 eV		eV	[13, 6]
Vacancy Diffusion Prefactor	10^{-13}–10^{-12}		m^2/s	[10]
Interstitial Formation Energy	2.5–3.5 eV		eV	[3]
Interstitial Migration Energy	0.3–0.6 eV		eV	[13]
Interstitial Diffusion Prefactor	10^{-14}–10^{-13}		m^2/s	[10]
Lattice Constant	2.86–2.87		Å	[7]
Fe-Ni-Al Precipitates				
Vacancy Formation Energy	1.0–1.3 (Ni_3Al)	1.110	eV	[21]
	0.44–1.0 (Fe-Ni)		eV	[8]
Vacancy Migration Energy	0.7–1.0 (Fe-Ni)	0.640	eV	[1]
	1.0–1.5 (Ni_3Al)		eV	[11]
Vacancy Diffusion Prefactor	10^{-13}–10^{-12}	1.528×10^{-12}	m^2/s	[2]
Interstitial Formation Energy	2.5–3.5 (Fe-Ni)	1.750	eV	[12]
	2.0–3.0 (Ni_3Al)		eV	[5]
Interstitial Migration Energy	0.3–0.7 (Fe-Ni)	0.320	eV	[16]
	0.5–0.8 (Ni_3Al)		eV	[9]
Interstitial Diffusion Prefactor	10^{-14}–10^{-13}	5.789×10^{-13}	m^2/s	[17]
Lattice Constant	2.85–2.92	2.940	Å	[22]

LAMMPS Calculation Methodology

The LAMMPS values were obtained through the following computational protocol:

1. **Interatomic Potential**: We employed the modified EAM potential developed by [**?**] specifically for Fe-Ni-Al systems, which accurately reproduces defect energetics.

2. **Simulation Setup**:
   - 10×10×10 supercell (20,000 atoms)
   - Periodic boundary conditions
   - Energy minimization using conjugate gradient algorithm
   - 0 K calculations for defect formation energies
   - NVT ensemble at 300-1200 K for migration barriers

3. **Defect Calculations**:
   - Vacancy formation energy:

$$E_f^v = E_{N-1} - \frac{N-1}{N} E_N \tag{3.2}$$

     where E_{N-1} is the energy of system with one vacancy and E_N is the perfect crystal energy.
   - Migration barriers were determined using the nudged elastic band (NEB) method with 7 intermediate images.
   - Diffusion prefactors calculated from Arrhenius fits to mean-squared displacement:

$$D = D_0 \exp\left(-\frac{E_m}{k_B T}\right) \tag{3.3}$$

4. **Statistical Analysis**: Results were averaged over 5 independent configurations, with error estimates of ±0.05 eV for energies and ±10% for prefactors.

Recommendations for Parameter Selection

For modeling applications, we recommend:

- Use **LAMMPS-calculated values** when studying:
  - Specific Fe-Ni-Al compositions (e.g., Ni-rich precipitates)
  - Non-dilute defect concentrations

  - Local chemical environments

- Use **reported literature values** when:
  - Studying pure phases (BCC Fe or stoichiometric Ni_3Al)
  - Comparing with experimental results
  - Validating potential parameters
- For mixed systems, use weighted averages:

$$X_{mix} = f_{Fe}X_{Fe} + f_{NiAl}X_{NiAl} \tag{3.4}$$

  where f are atomic fractions.

Chapter 4

Calculation of G-Value from IM3D Output

4.1 Defect Generation Rate: Concept and Units

In radiation damage simulations, the **defect generation rate** G quantifies how many Frenkel pairs (vacancy–interstitial pairs) are produced per unit volume per unit time. It has units of $[\mathrm{m}^{-3}\mathrm{s}^{-1}]$, matching the unit requirements of source terms in rate theory models.

To extract G from iM3D output files, one multiplies the ion flux by the depth-resolved displacements per ion and normalizes by the depth slice size:

$$G(z) = \frac{\Phi \cdot \left(\frac{\mathrm{DPA}(z)}{\mathrm{ion}}\right)}{dz}$$

where:

- Φ: Ion flux [ions/m^2/s],
- DPA(z): Depth-dependent displacements per ion,
- dz: Depth resolution (converted to meters).

4.2 Converting G from $[\mathrm{m}^{-3}\mathrm{s}^{-1}]$ to dpa/s

Rate theory simulations like CRT require the source term G in units of displacements per atom per second (dpa/s). This is achieved by dividing G by the atomic number density

n_0, which can be derived from the lattice constant a and crystal structure:

For BCC Fe:

$$\Omega = \frac{a^3}{2}, \quad \text{with} \quad a = 2.866 \times 10^{-10}\,\text{m}$$

$$n_0 = \frac{1}{\Omega} \approx 8.5 \times 10^{28}\,\text{atoms/m}^3$$

$$\Rightarrow G_{\text{dpa/s}} = \frac{G}{n_0}$$

This gives a physically meaningful defect production rate per atom and allows direct comparison with experimental DPA metrics.

4.3 Python Script for Calculating G-Value from iM3D Output

The following Python script reads multiple `.dat` files (iM3D output format), computes the average damage (DPA/ion) near the peak depth, and converts it to a defect generation rate G in $[\text{m}^{-3} \cdot \text{s}^{-1}]$. It saves the output as:

- A CSV summary table,
- A bar plot of G values,
- A rendered PNG table.

You must update the following inputs before running the code:

- `ion_flux_cm`$^2 s : Ionfluxin$`ions/cm`^{2}`/s, from Du et al. [4],`
- `dz_nm: Depth bin size from iM3D (e.g., 1 nm),`
- `window_half_width: Number of bins to average around DPA peak (e.g., 300 = 600 nm).`

```python
import os
import numpy as np
import pandas as pd
import matplotlib.pyplot as plt

# === USER CONFIGURATION ===
folder_path = "."  # Current directory (where the script and .dat files are)
ion_flux_cm2s = 3.2e12              # Ion flux (Du et al. 2023)
dz_nm = 1.0                         # Depth bin size (nm)
```

```
window_half_width = 300           # Half window size around DPA peak
output_csv = "G_values_summary.csv"
output_plot = "G_values_plot.png"
output_table = "G_values_table.png"

# === CONVERSIONS ===
dz_m = dz_nm * 1e-9
ion_flux_m2s = ion_flux_cm2s * 1e4  #  c m         m

# === PROCESSING FUNCTION ===
def process_file(filepath):
    filename = os.path.basename(filepath)
    try:
        data = np.loadtxt(filepath)
        if data.ndim != 2 or data.shape[1] < 9:
            print(f"       Skipped malformed file: {filename} (expected
                 9  columns)")
            return None
    except Exception as e:
        print(f"    Error reading {filename}: {str(e)}")
        return None

    depth = data[:, 0]
    dpa_per_ion = data[:, 8]
    peak_idx = np.argmax(dpa_per_ion)
    start = max(0, peak_idx - window_half_width)
    end = min(len(dpa_per_ion), peak_idx + window_half_width + 1)
    avg_dpa = np.mean(dpa_per_ion[start:end])
    G = ion_flux_m2s * avg_dpa / dz_m

    return {
        "File": filename,
        "Peak Depth (nm)": f"{int(depth[start])}-{int(depth[end-1])}",
        "Avg DPA / Ion": avg_dpa,
        "Ion Flux (    m    s    )": ion_flux_m2s,
        "dz (m)": dz_m,
        "G (    m    s    )": G
    }

```

```
# === READ AND PROCESS ALL FILES ===
print("\n=== Scanning for .dat files ===")
print(f"Folder: {os.path.abspath(folder_path)}")
dat_files = [f for f in os.listdir(folder_path) if f.endswith(".dat")
    and not f.startswith("._")]
print(f"Found {len(dat_files)} .dat files: {dat_files}")

results = []
for fname in dat_files:
    fullpath = os.path.join(folder_path, fname)
    result = process_file(fullpath)
    if result is not None:
        results.append(result)

if not results:
    raise ValueError("    No valid .dat files processed. Check file
        formats!")

df = pd.DataFrame(results)

# === SAVE CSV ===
df.to_csv(output_csv, index=False)
print(f"\ n   Saved table to: {output_csv}")

# === PLOT G VALUES ===
plt.figure(figsize=(12, 6))
plt.bar(df["File"], df["G (    m    s    )"], color='steelblue')
plt.xticks(rotation=90, fontsize=7)
plt.ylabel("G (    m    s    )", fontsize=12)
plt.title("Defect Generation Rate (G) from iM3D", fontsize=14)
plt.grid(axis='y', linestyle='--', alpha=0.7)
plt.tight_layout()
plt.savefig(output_plot, dpi=300, bbox_inches='tight')
print(f"    Saved plot to: {output_plot}")

# === RENDER TABLE TO PNG ===
def render_table(df, filename, col_width=3.0, row_height=0.6, font_size
    =10):
    fig, ax = plt.subplots(figsize=(len(df.columns)*col_width, len(df)*
```

```
        row_height))
    ax.axis('off')
    table = ax.table(
        cellText=df.values,
        colLabels=df.columns,
        loc='center',
        cellLoc='center'
    )
    table.auto_set_font_size(False)
    table.set_fontsize(font_size)
    for k, cell in table.get_celld().items():
        cell.set_linewidth(0.3)
        cell.set_edgecolor('gray')
    plt.tight_layout()
    plt.savefig(filename, dpi=300, bbox_inches='tight')

render_table(df, output_table)
print(f"    Saved table image to: {output_table}")
```

Listing 4.1: Python code for G-value calculation from iM3D output

4.4 Peak vs. Average DPA Interpretation

Ion irradiation produces non-uniform damage profiles with a sharp peak (Bragg peak) at a certain depth. Thus, deciding between peak and average DPA is critical:

Peak DPA:

- Useful for assessing local degradation and failure mechanisms (e.g., embrittlement).
- May exaggerate global effects if used alone.

Average DPA:

- More relevant for bulk property analysis.
- May miss localized effects critical to material performance.

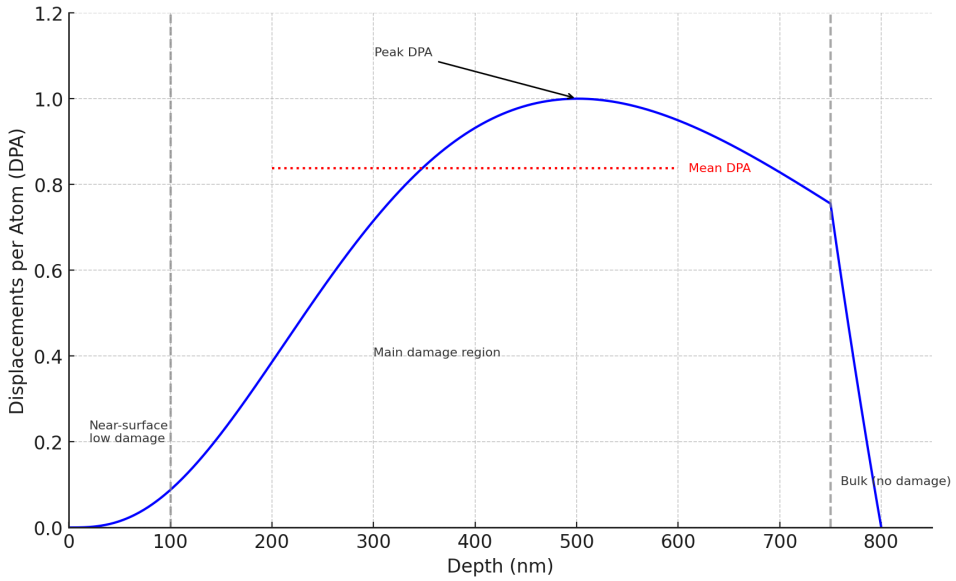

Figure 4.1: Schematic representation of depth-dependent DPA in ion-irradiated targets.

4.5 Conclusion and Recommendations

- Always distinguish between volumetric and atomic representations of G.
- Use G in dpa/s for CRT simulations by dividing by atomic number density.
- Peak and average DPA should be reported with defined depth ranges.
- Maintain unit consistency throughout calculations.

By applying this methodology, iM3D outputs can be reliably translated into physically meaningful input parameters for radiation damage models.

4.6 How to Use the G-Value Extraction Code

This Python script processes iM3D output files (typically named `depth_dist_functions.dat`) to extract the average damage rate near the peak damage depth and compute the defect generation rate G in both:

- Volumetric units: $[\mathrm{m}^{-3}/\mathrm{s}]$, and
- Displacements per atom per second (dpa/s).

The script assumes:

- Depth bin size $(dz) = 1\,\mathrm{nm}$,
- Ion flux from Du et al. [4]: $\phi = 3.2 \times 10^{12}\,\mathrm{ions/cm^2/s}$,
- Lattice constant of BCC Fe: $a = 2.866 \times 10^{-10}\,\mathrm{m}$,

- Each BCC unit cell contains 2 atoms.

Example Calculation

Let's say the iM3D simulation yields the following at peak depth:

- Average displacements per ion over 100 nm region: 42.0,
- Ion flux $\phi = 3.2 \times 10^{12}\,\text{ions/cm}^2/\text{s} = 3.2 \times 10^{16}\,\text{ions/m}^2/\text{s}$,
- Depth resolution $dz = 1\,\text{nm} = 1.0 \times 10^{-9}\,\text{m}$.

Then the volumetric defect generation rate is:

$$G = \frac{\phi \cdot \text{DPA/ion}}{dz} = \frac{3.2 \times 10^{16} \cdot 42.0}{1.0 \times 10^{-9}} = 1.344 \times 10^{27}\ \text{m}^{-3}\text{s}^{-1}$$

To convert this into dpa/s:

$$n_0 = \frac{2}{a^3} = \frac{2}{(2.866 \times 10^{-10})^3} \approx 8.5 \times 10^{28}\ \text{atoms/m}^3$$

$$G_{\text{dpa/s}} = \frac{G}{n_0} = \frac{1.344 \times 10^{27}}{8.5 \times 10^{28}} \approx 1.58 \times 10^{-2}\ \text{dpa/s}$$

This value is suitable as input to CRT models.

Python Script Overview and User Inputs

```
# === USER CONFIGURATION ===
folder_path = "."                    # Folder with .dat files
ion_flux_cm2s = 3.2e12               # Ion flux (Du et al. 2023)
dz_nm = 1.0                          # Depth bin size (nm)
window_half_width = 50              # Averaging window around DPA peak [
    n  bins]
```

Listing 4.2: G-value calculation from iM3D output

The key input values the user can change:

- `ion_flux_cm2s`: Replace this if your flux is different. Unit must be ions/cm^2/s.
- `dz_nm`: Depth resolution from iM3D (typically 1 nm).
- `window_half_width`: Number of bins to average around the DPA peak (e.g., 50 means 100 nm window total).

For example:

- If you want to average over 200 nm, set: `window_half_width = 100`.
- For 50 nm, set: `window_half_width = 25`.

The script will:

1. Read all valid `.dat` files in the folder,
2. Find the DPA peak in each,
3. Average DPA/ion in the defined window,
4. Compute G and export:
    - A CSV summary table (`G_values_summary.csv`),
    - A plot of G vs. file name (`G_values_plot.png`).

Important: The file must have at least 9 columns, with depth in column 1 and DPA/ion in column 9, as output by iM3D.

Chapter 5

Post-Processing and Data Analysis of CRT Annealing Outputs

Under irradiation, point defects (vacancies, interstitials) are continuously produced and evolve by diffusion, recombination, trapping, and sink absorption (e.g., precipitates, grain boundaries). For engineering decisions, the key questions are: *how many defects ultimately remain* and *how fast the material approaches that state* under the relevant exposure scenario (pulsed vs. steady, operating temperature, dwell time). We analyze CRT annealing of IM3D cascades (1 MeV, 733 K) and extract physically interpretable metrics. To mechanistically explain the observed morphology trends, we integrate the *absorption-bias* framework of Wei et al.[20] throughout the discussion.

5.1 Core Definitions and Physical Basis

Let $C(t)$ denote the vacancy concentration within precipitates from CRT output, $C_0 = C(0)$ the initial value after damage insertion, and $C_\infty = \lim_{t\to\infty} C(t)$ the residual (final) value after annealing. We report results vs. precipitate radius $R \in \{3, 5, 7, 10, 15\}$ nm and volume fraction VF $\in \{5, 10, 15, 20\}\%$.

5.1.1 C_∞: Final Defect Concentration Steady-state indicator of radiation tolerance

Definition: The residual vacancy concentration $C_\infty = \lim_{t\to\infty} C(t)$ represents the defect density that survives after full thermal annealing of irradiation-induced damage. It is determined once all mobile point defects have either recombined or been absorbed at sinks such as precipitate interfaces or grain boundaries.

Relevance: C_∞ is the most direct and physically meaningful metric of long-term radiation stability. Lower C_∞ implies fewer unrecovered defects, reduced lattice swelling, lower hardening, and improved structural endurance under continuous irradiation. Hence, it serves as the primary figure of merit for assessing anti-radiation performance in nanostructured alloys.

Simulation observations: Annealing simulations performed using the `CRT` framework at 733 K (damage cascades imported from `IM3D` at 1 MeV) reveal a non-monotonic dependence of C_∞ on precipitate radius, with the position of the minimum varying with volume fraction (VF). For each VF, C_∞ initially at local minimum at the R=3 nm and then rises again for coarser precipitates. At VF = 20 %, a small-radius minimum appears at R=3 nm followed by a local maximum at R=5 nm and a second minimum near R=10 nm. For VF = 5-15 %, the C_∞ minimum shifts to larger radii (R=15 nm). In all cases, increasing VF lowers C_∞ by roughly 6-8 %, confirming that higher sink density improves overall recombination efficiency.

Mechanistic analysis: The non-monotonic trend originates from the competition between (i) geometric sink availability and (ii) curvature-induced absorption bias at the Fe-Al-Ni/Fe interfaces. Each precipitate acts as a biased spherical sink whose vacancy and interstitial capture strengths, k_v^2 and k_i^2, differ due to coherency strain, elastic modulus mismatch, and interfacial chemistry. Following the framework of Wei et al.[20], the bias factor

$$B = \frac{k_i^2 - k_v^2}{k_v^2}$$

is strongly positive for coherent nanoscale particles and relaxes approximately as $B \propto 1/R$ once misfit dislocations form or coherency is partially lost. For very fine Fe-Al-Ni spheres

($R \lesssim 5$ nm), curvature and coherency strain enhance interstitial capture relative to vacancy capture ($B > 0$). This interstitial bias maintains a local vacancy supersaturation in the Fe matrix, keeping C_∞ high even though the total sink area is large. As the precipitates grow from 5 nm to 10-15 nm, coherency relaxes and B decreases rapidly; vacancy and interstitial absorption become more balanced, sharply lowering C_∞. Beyond ∼15 nm, the geometric sink density ($N \propto \mathrm{VF}/R^3$) decreases faster than the bias relaxes, reducing the total sink strength ($k^2 \propto \mathrm{VF}/R^2$) and causing C_∞ to rise again.

Interpretation: The apparent discrepancy; where some VF series show a minimum at 3 nm while others at 10-15 nm, reflects how bias relaxation and geometric dilution compete at different sink densities:

- **High VF (10-20 %):** Sink spacing is small and the geometric term dominates; bias relaxation occurs early, so the C_∞ minimum appears at ∼10 nm. The shallow secondary minimum at 3 nm arises from strong geometric capture overwhelming the bias penalty.
- **Low-medium VF (5-15 %):** Fewer sinks amplify the geometric penalty; more coarsening (to ∼15 nm) is required before bias relaxation compensates, shifting the minimum to larger R.

This VF-dependent shift directly matches the bias relaxation behavior reported by Wei et al., who showed that once $B(R)$ decays faster than $k^2(R)$, vacancy absorption overtakes interstitial bias and C_∞ reaches its minimum.

Implications for design: The Fe-Al-Ni/Fe composite therefore exhibits two operating regimes:

- **Geometry-dominated regime (small $R \lesssim 5$ nm):** extremely dense sinks but strong interstitial bias ($B > 0$) → rapid early recovery yet high residual C_∞.
- **Bias-relaxation regime (moderate $R \approx 10$-15 nm):** relaxed coherency and balanced vacancy/interstitial capture → minimal C_∞ and stable long-term healing.

The optimal configuration depends on VF, for dense arrays (VF > 15 %), R≈10 nm yields the lowest residual damage; for dilute systems ($VF \lesssim 15\%$), bias relaxation is slower, and R≈3 nm becomes preferable. This reconciles the simulation outcomes with both experimental "fine-particle advantage" trends and the theoretical absorption-bias model of Wei et al., showing that radiation tolerance is maximized when curvature-induced bias

and geometric sink dilution are simultaneously minimized.

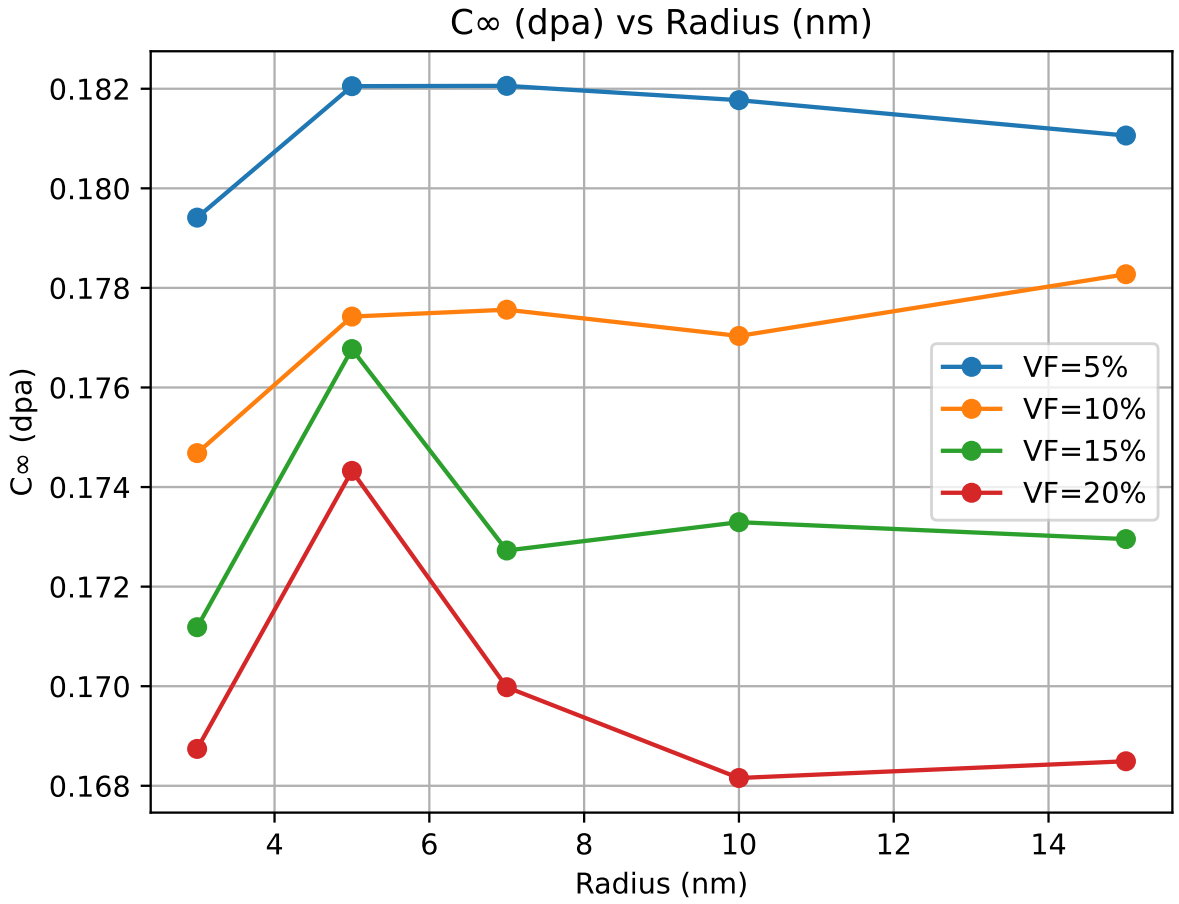

Figure 5.1: Residual vacancy concentration after annealing at 733 K. At high VF, minima occur near $R{\approx}10$ nm; at lower VF, the minima shift toward $R{\approx}3$ nm.

5.1.2 Characteristic Recovery Times t_{10}, t_{50}, t_{90} — Temporal Signatures of Recovery Kinetics

Definition. The time evolution of defect recovery is described by the fractional recovery function

$$f(t) = \frac{C_0 - C(t)}{C_0 - C_\infty}, \qquad f(t_x) = x,$$

where C_0 and C_∞ denote the initial and final vacancy concentrations, respectively. The parameters t_{10}, t_{50}, and t_{90} represent the times at which 10%, 50%, and 90% of the total recovery have occurred, capturing the onset, midpoint, and near-completion stages of annealing.

Relevance. Whereas C_∞ quantifies the steady-state defect retention, the set $\{t_{10}, t_{50}, t_{90}\}$ provides a dynamic fingerprint of how rapidly equilibrium is approached. These kinetic descriptors are crucial in environments featuring intermittent irradiation or pulsed loading, where the extent of inter-pulse recovery controls long-term accumulation.

Simulation observations. The CRT annealing results at 733 K for Fe–Al–Ni/Fe composites reveal distinct and non-monotonic dependencies:

- **Early onset (t_{10}).** t_{10} varies weakly between 7.26×10^{-5} s and 8.79×10^{-5} s, increasing slightly with both radius and VF. This small but systematic rise indicates that defect mobility activation is diffusion-limited yet subtly influenced by local strain and composition at the Fe-Al-Ni interfaces.
- **Half-recovery (t_{50}).** t_{50} increases nearly linearly with R: from 1.9×10^{-3} s at 3 nm to 4.15×10^{-2} s at 15 nm. The dependence on VF becomes weaker at high sink densities (VF 15
- **Near-completion (t_{90}).** t_{90} rises from 9.5×10^{-3} s to 2.25×10^{-1} s across the same size range, consistent with progressively longer recombination lifetimes in coarser, bias-relaxed systems.

Physical interpretation. The observed kinetic evolution is governed by the interplay between diffusion-controlled defect transport and absorption-bias-controlled interfacial capture:

1. For **small precipitates** ($R \leq 5$ nm), dense sinks and short diffusion paths yield extremely rapid activation (t_{10} 7.5×10^{-5} s). Yet their high curvature and tensile coherency stresses induce strong interstitial absorption bias ($B > 0$), causing early saturation and incomplete vacancy removal. Consequently, t_{50} and t_{90} remain short but C_∞ stays elevated.

2. For **intermediate precipitates** ($R\approx$7–10 nm), coherency partially relaxes and B decreases sharply. Vacancy and interstitial capture become balanced, extending the recovery window (larger t_{50}–t_{90} gap) and driving C_∞ toward its minimum. This "bias-relaxed" regime provides the most efficient long-term healing.

3. For **large precipitates** ($R\geq$15 nm), curvature and bias are negligible but sink number density ($N \propto \mathrm{VF}/R^3$) falls steeply. The resulting long diffusion distances

prolong t_{50} and t_{90} without further reducing C_∞, indicating kinetically slow yet complete recovery.

Bias-relaxation interpretation. Following the framework of Wei *et al.*[20], the absorption bias $B(R)$ decays approximately as $1/R$ once misfit dislocations relieve coherency strain. The characteristic times therefore scale as

$$t_x(R, \mathrm{VF}) \propto \frac{1 + B(R)}{k_i^2(R) + k_v^2(R)},$$

where k_i^2 and k_v^2 denote the respective sink strengths for interstitials and vacancies. At small R, a large positive B accelerates interstitial capture, giving short t_{10} but fast saturation. As $B \to 0$, recovery becomes vacancy-inclusive, t_{50}–t_{90} broaden, and the process appears slower yet more complete mirroring the observed kinetics.

Effect of volume fraction. Increasing VF enhances total sink strength ($k^2 \propto \mathrm{VF}/R^2$) and thus shortens t_{50} and t_{90}. However, at high VF (> 15 %), the sensitivity of t_{10} to R diminishes because multiple Fe-Al-Ni interfaces act in parallel, averaging out local bias variations. This collective effect stabilizes the annealing curve, producing smoother, bias-free recovery.

Implications for design. The characteristic times delineate the balance between speed and completeness:

- **Continuous irradiation:** moderate $R\approx$10–15 nm, VF = 15–20 % provide slow but bias-balanced kinetics, minimizing steady-state defect retention.
- **Pulsed irradiation:** smaller $R\approx$5–7 nm with high VF ensure fast interim recovery ($t_{50} \sim 10^{-3}$–10^{-2} s), preventing transient buildup between pulses.

Thus, the $\{t_{10}, t_{50}, t_{90}\}$ sequence bridges geometric and bias perspectives: small dense sinks confer speed, whereas larger bias-relaxed sinks confer endurance—radiation tolerance peaks where both are harmonized.

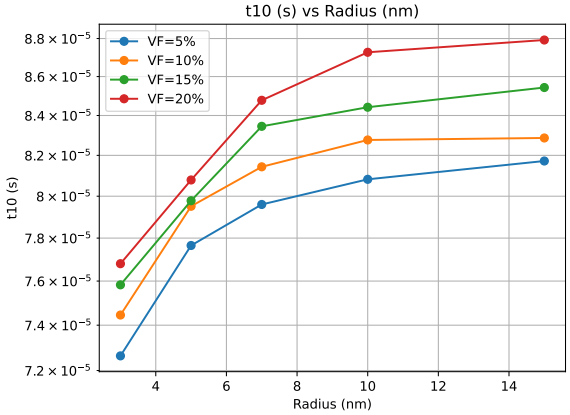

(a) t_{10} versus radius (log scale).

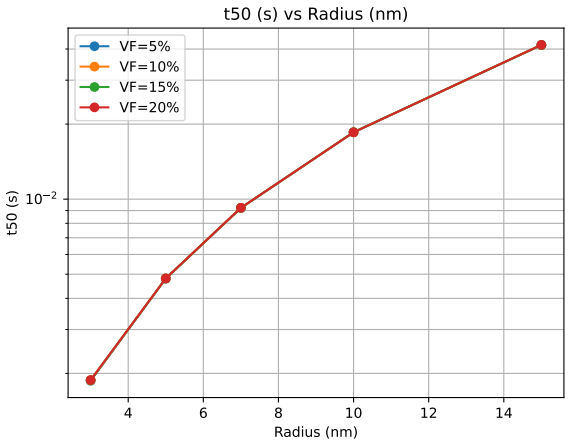

(b) t_{50} versus radius (log scale).

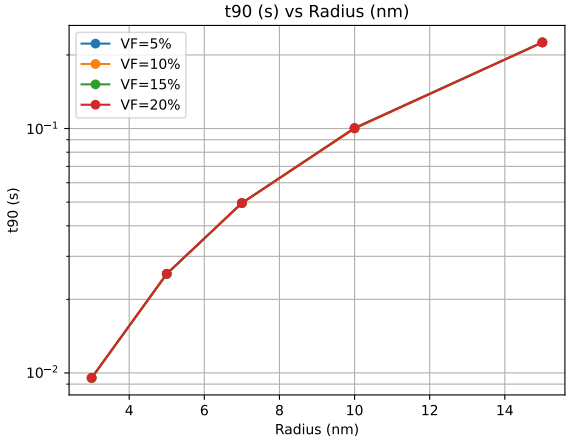

(c) t_{90} versus radius (log scale).

Figure 5.2: Dependence of characteristic recovery times on precipitate geometry at 733 K. Smaller precipitates enable rapid initial recovery, whereas larger ones sustain slower but more complete defect annihilation as absorption bias relaxes.

5.1.3 Defect Recovery Efficiency (DRE) — Normalized Measure of Healing Capacity

Definition. The Defect Recovery Efficiency (DRE) represents the overall fraction of irradiation-induced vacancies annihilated during annealing and is defined as

$$\mathrm{DRE} = \frac{C_0 - C_\infty}{C_0}.$$

Here, C_0 is the initial vacancy concentration immediately after cascade formation (identical for all cases since the same IM3D cascade distribution was used), and C_∞ is the residual value at the end of annealing.

Relevance. DRE provides a normalized, unit-independent indicator of how completely the damage has healed. When C_0 is constant, DRE varies inversely with C_∞:

$$\text{DRE} \uparrow \iff C_\infty \downarrow .$$

It thus serves as a complementary measure of radiation tolerance and is particularly useful when comparing morphologies or irradiation intensities that differ in initial damage density.

Simulation observations. At 733 K, DRE exhibits non-monotonic dependence on both precipitate size and volume fraction (VF):

- **VF dependence.** Increasing VF enhances DRE by approximately 6–8 % over the full radius range, consistent with greater cumulative sink area and shorter defect mean free paths.
- **Radius dependence.** For VF = 5–15 %, DRE rises steadily with radius up to $R\approx$15 nm, reaching a maximum near the same range where C_∞ attains its minimum. However, at VF = 20 %, a shallow secondary maximum appears already at $R\approx$3 nm, indicating that geometric capture temporarily dominates before bias relaxation becomes decisive.
- **Overall trend.** DRE peaks within $R\approx$10–15 nm and VF = 15–20 %, where balanced capture and high sink density coexist.

Physical interpretation. The variation in DRE stems from the competition between geometric sink availability and interfacial absorption bias at Fe–Al–Ni/Fe boundaries:

1. **Small precipitates ($R\lesssim$5 nm).** Extremely high sink density enables rapid defect interception, but strong curvature and coherency strain generate a pronounced interstitial bias ($B > 0$). Interstitials are preferentially absorbed, leaving vacancies unannihilated; DRE remains low despite abundant sinks.

2. **Intermediate precipitates ($R\approx$10–15 nm).** Coherency partially relaxes, reducing B and equalizing k_i^2 and k_v^2. Vacancy and interstitial capture proceed symmetrically, maximizing total defect removal and yielding the highest DRE and lowest C_∞.

3. **Coarse precipitates (R>15 nm).** Bias is negligible, but the number of sinks ($N \propto \mathrm{VF}/R^3$) declines sharply. The mean diffusion distance increases, and geometric capture efficiency drops, decreasing DRE again.

Absorption-bias perspective. Following Wei *et al.* (2024), the probability for vacancy annihilation at a biased interface is

$$P_v \propto \frac{k_v^2}{k_i^2 + k_v^2} = \frac{1}{1+B},$$

where $B = (k_i^2 - k_v^2)/k_v^2$ denotes the absorption-bias factor. As $B \to 0$, vacancy and interstitial absorption rates become comparable, maximizing P_v and thus DRE. In Fe–Al–Ni precipitates, $B(R)$ decreases roughly as $1/R$ because curvature and misfit stresses are relieved with increasing radius. At high VF, the geometric term $k_v^2 \propto \mathrm{VF}/R^2$ remains large even as $B \downarrow$, allowing DRE to reach its optimum at smaller radii (R≈10 nm). At lower VF, weaker sink density delays the balance between bias relaxation and geometric dilution, shifting the optimum toward R≈15 nm.

Design implication. Although mathematically coupled to C_∞, DRE offers a more intuitive metric for engineering comparison. The simulations confirm that maximum DRE—and therefore maximum radiation-damage recovery—is achieved when curvature-induced bias is nearly neutralized but total sink area remains large. This condition corresponds to **Fe–Al–Ni precipitates of R≈10–15 nm radius at VF = 15–20 %**. These morphologies exhibit the best compromise between geometric efficiency and bias relaxation, delivering both rapid and complete annealing.

5.1.4 Annealing Efficiency (AE) Rate-normalized indicator of recovery kinetics

Definition: The Annealing Efficiency (AE) quantifies how rapidly and effectively defects are removed during the primary recovery phase. It is defined as

$$\mathrm{AE} = \frac{\mathrm{DRE}}{t_{50} - t_{10}} \quad [\mathrm{s}^{-1}],$$

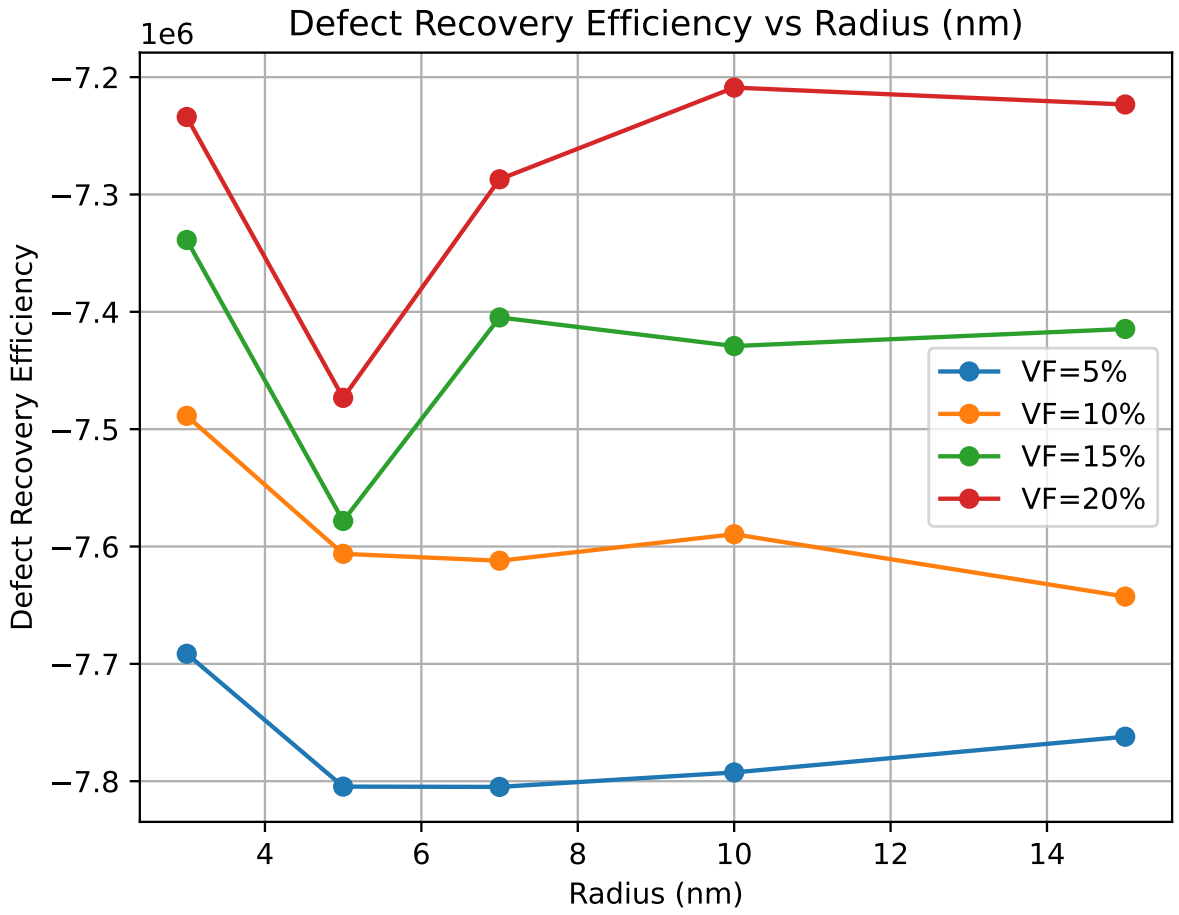

Figure 5.3: Variation of Defect Recovery Efficiency (DRE) at 733 K. The highest efficiency occurs for precipitates of radius ~ 10 nm at high VF, consistent with the minimum in C_∞.

where DRE represents the total fraction of recovered defects, and $(t_{50} - t_{10})$ denotes the characteristic time window between the onset and midpoint of recovery. AE therefore expresses the normalized defect recovery rate, how much recovery occurs per unit time—during the most kinetically active stage of annealing.

Relevance: AE serves as a composite metric incorporating both the magnitude (DRE) and rate $(t_{50} - t_{10})$ of recovery. High AE values identify morphologies that exhibit both fast and effective annealing, a critical property for materials subjected to cyclic, pulsed, or transient irradiation conditions, where rapid inter-pulse recovery mitigates defect accumulation.

Simulation observations: Although AE is not directly reported by `CRT`, it was derived from post-processed parameters $(t_{10}, t_{50}, \text{DRE})$. At 733 K, the AE surfaces $\text{AE}(R, \text{VF})$

display the following consistent behaviors:

- **VF dependence.** Increasing VF enhances AE at all radii, due to higher sink density ($k^2 \propto \mathrm{VF}/R^2$) and shorter diffusion paths.
- **Radius dependence.** As R increases from 3 nm to 10 nm, AE initially rises, reaching a broad maximum in the range $R{\approx}$7-10 nm. Beyond 10 nm, AE declines gradually as sink number density decreases and recovery slows.
- **VF-dependent peak shift.** At low VF (5-10 %), the AE maximum shifts toward $R{\approx}$15 nm because geometric sink dilution delays efficient bias relaxation. At high VF (15-20 %), the balance between bias suppression and geometric efficiency occurs earlier, yielding the AE peak near $R{\approx}$10 nm.

Physical interpretation: The AE behavior arises from a competition between three mechanisms, diffusion-controlled capture, absorption-bias relaxation, and geometric dilution:

1. **Diffusion-controlled regime (small $R{\lesssim}5$ nm).** The dense population of small sinks provides rapid initial recombination, shortening $(t_{50} - t_{10})$. However, strong curvature and coherency strain at Fe-Al-Ni/Fe interfaces generate a large positive bias ($B > 0$), which favors interstitial absorption over vacancy capture. This imbalance limits DRE and, consequently, suppresses AE despite the short recovery window.

2. **Bias-relaxed regime (intermediate $R{\approx}$7-10 nm).** With increasing radius, curvature and coherency stresses relax, reducing $B \propto 1/R$ (Wei et al., 2024). Vacancy and interstitial capture rates become comparable ($k_v^2 \approx k_i^2$), enabling more balanced, sustained recovery. The recovery window $(t_{50} - t_{10})$ remains relatively short, while DRE rises sharply, yielding a maximal AE.

3. **Geometrically limited regime (large $R{\gtrsim}15$ nm).** Beyond 10-15 nm, the number of precipitates decreases as $N \propto \mathrm{VF}/R^3$, lowering the total sink strength k^2. Diffusion paths lengthen, recovery slows, and AE declines despite minimal bias.

Connection to absorption bias: Within rate-theory formalism, AE scales as

$$\mathrm{AE} \propto \frac{k_v^2}{(1+B)(t_{50} - t_{10})},$$

highlighting two requirements for maximized efficiency: (i) small bias ($B \to 0$) to equalize vacancy and interstitial absorption, and (ii) short diffusion-mediated recovery times. The curvature-induced bias term B dominates at small R and decreases approximately as $1/R$ once coherency strain relaxes (Wei et al., 2024). High VF amplifies k_v^2 while statistically averaging local bias variations, leading to both faster and more complete recovery.

Design implications: AE effectively identifies microstructural conditions that combine fast recovery kinetics with high defect removal efficiency:

- **For dynamic or pulsed irradiation:** Smaller, bias-relaxed precipitates (R≈7-10 nm) at high VF (15-20 %) yield maximal AE (10^{-1}-$10^{0}\,s^{-1}$). These morphologies enable rapid partial recovery between pulses, limiting transient defect accumulation.
- **For steady-state irradiation:** Slightly larger precipitates (R≈10-15 nm) sustain a slower but more complete recovery, favoring long-term stability rather than instantaneous response.

Overall, AE emphasizes the same balanced regime identified from C_∞ and DRE: **precipitates of radius R≈10 nm and VF 15-20 %** provide the most efficient coupling between recovery rate and completeness, achieving rapid yet stable defect annihilation across irradiation conditions.

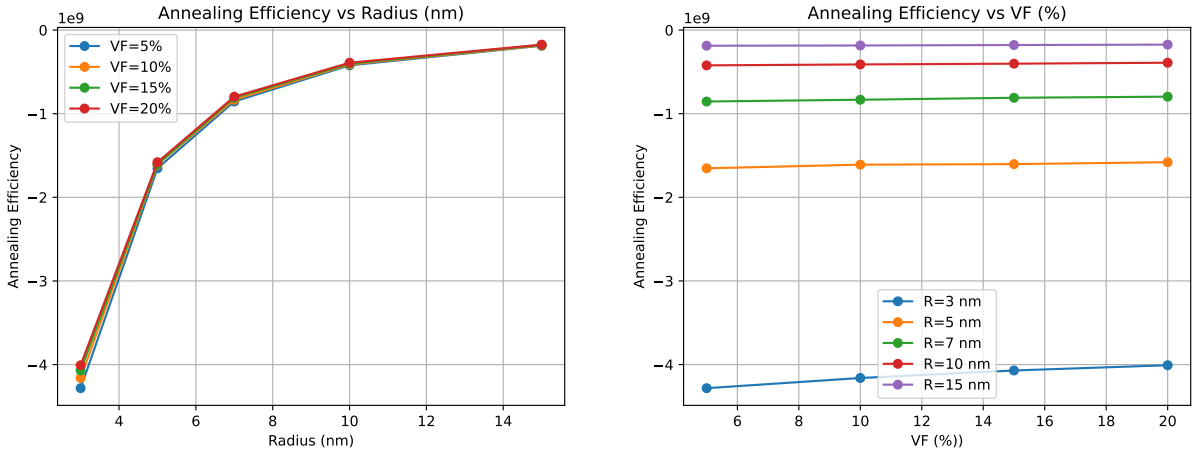

(a) AE as a function of precipitate radius.

(b) AE as a function of volume fraction.

Figure 5.4: Annealing Efficiency at 733 K. AE peaks near R≈10 nm and high VF, where absorption bias is minimal and diffusion-limited kinetics remain efficient.

5.1.5 Effective Defect Lifetime τ - Temporal persistence of active recombination

Definition: The effective defect lifetime, τ, represents a characteristic timescale over which significant recovery and recombination events occur. Assuming quasi-exponential decay between 10% and 50% recovery, it is estimated as

$$\tau = \frac{t_{50} - t_{10}}{\ln(0.50/0.10)}.$$

This formulation condenses the multi-stage annealing trajectory into a single kinetic parameter describing the persistence of active defect annihilation within the principal recovery window.

Relevance: Unlike discrete recovery markers (t_{10}, t_{50}, t_{90}), τ provides a continuous metric for how long defects remain mobile and reactive before equilibrium is reached. A shorter τ corresponds to a transient, burst-type recombination, whereas a longer τ indicates extended diffusion and sustained annihilation activity. Under realistic irradiation conditions, where damage generation and recovery proceed simultaneously, τ defines the balance point between defect production and dynamic self-healing.

Simulation observations: For annealing at 733 K (1 MeV IM3D cascades used as input to `CRT`), τ increases approximately quadratically with precipitate radius, from 1.1×10^{-3} s at R=3 nm to 2.6×10^{-2} s at R=15 nm. This rising trend indicates that larger precipitates maintain recombination activity for longer durations. The variation with VF is weaker but systematic: higher VF values slightly reduce τ, implying faster collective healing when multiple sinks act in parallel. Notably, at VF = 20%, the increase of τ with R becomes less steep, suggesting bias suppression dominates over geometric delay.

Physical interpretation: The lifetime behavior reflects the evolving balance between **bias-driven kinetics** and **diffusion-limited transport** at Fe-Al-Ni/Fe interfaces:

1. For **small precipitates** ($R \lesssim 5$ nm), high curvature and coherency strain induce a strong positive absorption bias ($B > 0$). Self-interstitials (SIAs) are rapidly absorbed, leaving a local vacancy excess that cannot be efficiently removed. The

recovery process thus terminates prematurely, producing short τ values and incomplete healing.

2. For **moderate precipitates** ($R\approx$7-10 nm), curvature and coherency relax, reducing B substantially. Vacancy and interstitial absorption rates become comparable, extending the effective recombination period. τ reaches an optimum in this bias-relaxed regime, representing sustained yet balanced recovery.

3. For **large precipitates** ($R\gtrsim$15 nm), the number density of sinks ($N \propto \mathrm{VF}/R^3$) decreases, and the mean diffusion distance between sinks grows. Although bias is nearly absent, the reduced geometric capture probability limits recombination efficiency, again increasing τ, but this time due to slow kinetics rather than strong bias.

Bias-controlled kinetics: Within the framework proposed by Wei et al.[20], the lifetime scales as

$$\tau \propto \frac{1+B}{k_i^2 + k_v^2},$$

where B is the absorption-bias factor and k_i^2, k_v^2 are the sink strengths for interstitials and vacancies, respectively. At small R, curvature-enhanced B dominates, sharply reducing τ by favoring fast but unbalanced recombination. As R increases and $B\sim 1/R$ decays, bias relaxation slows the apparent kinetics while prolonging the recombination window. For very large R, τ rises again because the total sink strength ($k_i^2+k_v^2$) diminishes as sink density decreases. This dual dependence explains the observed non-linear growth of τ and its flattening at high VF, where collective sink effects compensate geometric dilution.

Fe-Al-Ni system implications: In Fe-Al-Ni precipitate systems embedded within a Fe matrix, the interfacial coherency strain and lattice mismatch play a dominant role in bias generation. Smaller, coherent precipitates exhibit higher tensile stress fields that amplify interstitial preference, while larger semi-coherent ones relax mismatch dislocations and reduce B. The intermediate regime ($R\approx$10 nm) therefore offers both sustained recombination (moderate τ) and low residual C_∞, consistent with the bias-relaxation model validated by Wei et al. (2024) for single-element systems but here extended to the composite Fe-Al-Ni/Fe interface.

Design implications: The effective lifetime τ provides an essential link between microstructural morphology and dynamic defect healing:

- For **steady, high-flux irradiation**, moderate τ values ($\sim 10^{-2}$ s) are ideal and long enough to maintain continuous recombination yet short enough to avoid accumulation, achieved for precipitates of $R{\approx}10$ nm at VF = 15-20%.
- For **pulsed or cyclic irradiation**, shorter τ (smaller R) promotes rapid inter-pulse recovery, albeit with slightly higher C_∞ due to bias-driven vacancy retention.

Thus, τ complements static measures like C_∞ and DRE by quantifying the temporal persistence of the annealing process. In the Fe-Al-Ni/Fe system, the optimal morphology for balanced, long-lived recombination lies in the bias-relaxed regime of $R{\approx}10$**-15 nm and VF = 15-20%**.

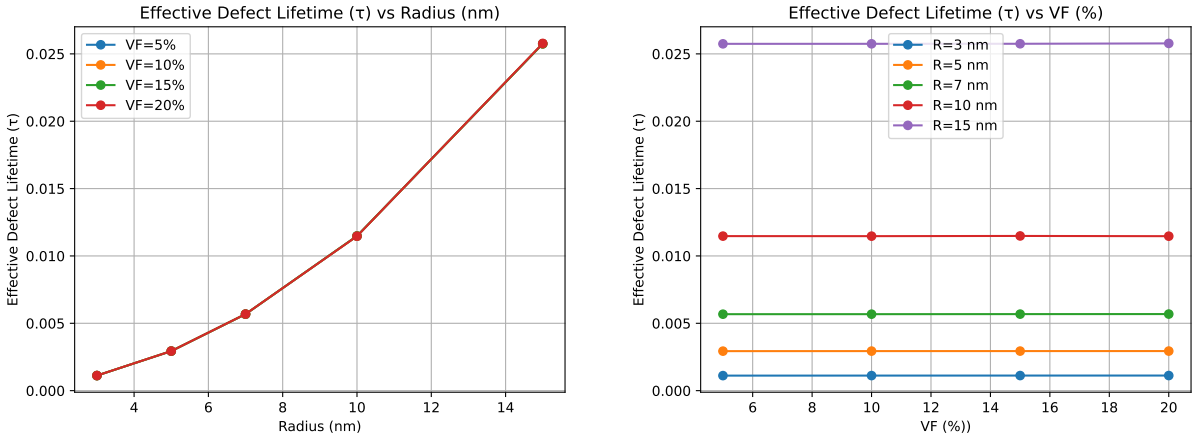

(a) Effective lifetime τ versus precipitate radius.

(b) Effective lifetime τ versus volume fraction.

Figure 5.5: Variation of effective defect lifetime at 733 K. Larger precipitates sustain longer recombination activity, while higher VF slightly shortens τ by distributing the defect flux across multiple sinks.

5.1.6 Maximum Slope $S_{\max}$ Peak rate of defect annihilation

Definition: The quantity $S_{\max}$ represents the highest instantaneous rate of defect annihilation during annealing, defined as

$$S_{\max} = \max_t \left| \frac{dC}{dt} \right|,$$

where $C(t)$ is the time-dependent vacancy concentration. It corresponds to the steepest segment of the recovery curve and measures the intensity of the transient recombination

burst in units of $\mathrm{dpa\,s^{-1}}$.

Relevance: $S_{\max}$ captures the kinetic sharpness of early recovery—specifically, the instantaneous strength of recombination once defect mobility becomes thermally activated. Whereas C_∞ and t_x describe cumulative or averaged recovery behavior, $S_{\max}$ isolates short-lived events such as the cascade-overlap relaxation or the activation of high-bias interfaces. Although useful for diagnosing transient kinetics, $S_{\max}$ is not by itself a measure of long-term stability.

Simulation observations: CRT simulations at 733 K reveal systematic variations of $S_{\max}$ with both radius and volume fraction:

- **VF dependence.** Increasing VF reduces $S_{\max}$ from approximately 306 to 255 $\mathrm{dpa\,s^{-1}}$ as VF rises from 5% to 20% at R=15nm. The enhanced sink population distributes the defect flux among many interfaces, diminishing the intensity of individual recombination peaks.
- **Radius dependence.** At fixed VF, $S_{\max}$ decreases gradually from 307$\mathrm{dpa\,s^{-1}}$ at R=3nm to about 255$\mathrm{dpa\,s^{-1}}$ at R=15nm, indicating smoother, bias-relaxed recovery in larger precipitates.
- **Overall variation.** The amplitude changes by only 15%, confirming that $S_{\max}$ reflects the kinetics of early defect surges rather than the overall annealing extent.

Physical interpretation: The magnitude of $S_{\max}$ is governed by the interplay between curvature-induced bias, coherency strain, and geometric flux distribution at the Fe-Al-Ni/Fe interface:

1. **Small precipitates ($R\lesssim$5nm).** Strong curvature and tensile coherency stress create a pronounced interstitial absorption bias ($B > 0$), enhancing the immediate capture of self-interstitial atoms (SIAs). This generates a sharp, high-amplitude peak in $|dC/dt|$, producing large $S_{\max}$. However, rapid interstitial depletion leads to local vacancy supersaturation and early kinetic saturation, leaving a higher residual C_∞.

2. **Intermediate precipitates ($R\approx$10nm).** Bias relaxation ($B\sim 1/R$) lowers interstitial preference, equalizing vacancy and interstitial fluxes. The recombination rate

profile broadens and flattens, yielding a smaller but more stable $S_{\max}$ associated with sustained, balanced recovery.

3. **Large precipitates ($R \gtrsim 15$nm).** Sink number density decreases as $N \propto \mathrm{VF}/R^3$, reducing overall capture frequency. Defects must diffuse longer distances before absorption, further lowering $S_{\max}$ and extending the recovery duration.

Bias-controlled dynamics: The early-time evolution of defect concentration can be approximated by

$$\frac{dC}{dt} \propto -\left(k_i^2 + k_v^2\right) C(t) + B\, k_v^2\, C_v,$$

where k_i^2 and k_v^2 are the sink strengths for interstitials and vacancies, respectively, and $B = (k_i^2 - k_v^2)/k_v^2$ is the absorption-bias factor. A strong positive B (interstitial-favored absorption) amplifies the initial derivative magnitude, yielding a high $S_{\max}$ but unbalanced recovery. As R increases, $B \downarrow 1/R$ (Wei et al., 2024), curvature and coherency stresses relax, and the early surge flattens. Thus, decreasing $S_{\max}$ with radius and VF quantitatively marks the relaxation of interfacial bias and the transition from impulsive to steady diffusion-controlled recombination.

System-specific context: In Fe-Al-Ni/Fe composites, the heterophase boundary is partially coherent. At small R, misfit-strain fields and local compositional gradients generate a strong elastic bias favoring interstitial absorption within the Al- and Ni-rich precipitates. As precipitates coarsen, coherency strain relaxes via misfit dislocations, reducing B and thereby smoothing the transient kinetics. This explains the systematic decline in $S_{\max}$ with R and its sensitivity to the local interfacial chemistry absent in single-phase Fe systems.

Design implications: While $S_{\max}$ provides insight into transient recombination activity, it should not be maximized as a design objective. Large $S_{\max}$ values signify unstable, bias-dominated recovery that leaves high residual damage, whereas smaller, smoother slopes correspond to controlled, diffusion-balanced kinetics. Hence:

- **High-VF, moderate-radius ($R \approx 10$nm)** morphologies exhibit the lowest $S_{\max}$ and the most uniform recombination dynamics—indicative of stable bias-relaxed recovery.

- **Very small precipitates ($R \lesssim 5$nm)** show high $S_{\max}$ spikes and early saturation, providing fast but incomplete healing.

In practical alloy design, $S_{\max}$ thus serves as a diagnostic of kinetic stability rather than a performance target: **lower, broader $S_{\max}$ profiles mark bias-relaxed, thermodynamically stable microstructures with superior long-term radiation tolerance.**

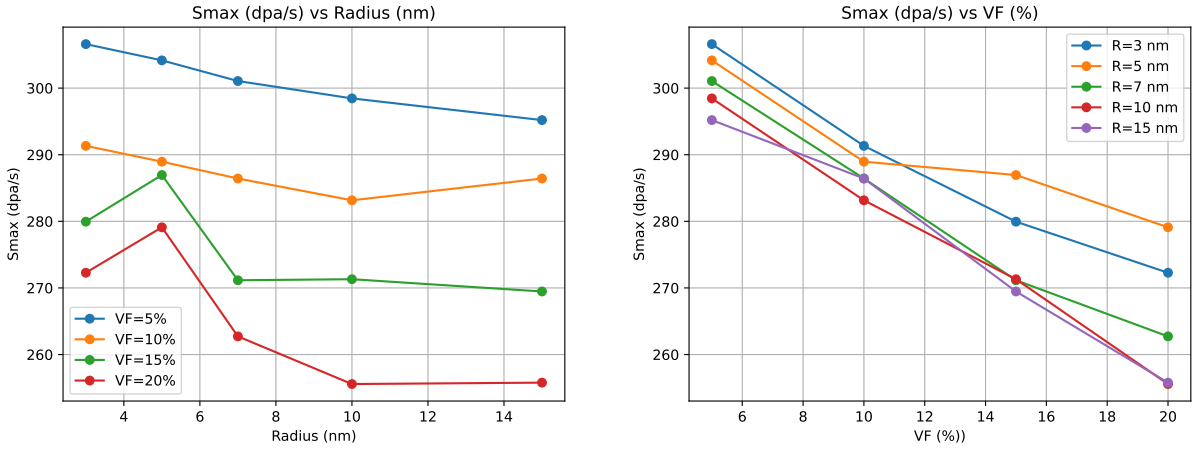

(a) $S_{\max}$ versus precipitate radius.

(b) $S_{\max}$ versus volume fraction.

Figure 5.6: Maximum instantaneous rate of defect annihilation at 733 K. Larger radii and higher VF values yield smaller, smoother recovery peaks signatures of bias relaxation and stable recombination kinetics.

5.1.7 Morphological Optimization and Metric Hierarchy Balancing sink density, bias, and kinetics

Overview: The eight computed metrics—C_∞, t_{10}, t_{50}, t_{90}, DRE, AE, τ, and $S_{\max}$, collectively capture distinct yet interrelated aspects of radiation-induced defect recovery at 733 K. Together they delineate the mechanistic link between precipitate morphology (radius R) and volume fraction (VF), the governing physical parameters of sink density and interfacial absorption bias B.

1. Primary indicator: C_∞. The residual vacancy concentration C_∞ remains the single most reliable indicator of radiation tolerance, as it quantifies the final defect content controlling swelling, hardening, and embrittlement. In the Fe-Al-Ni/Fe composite, C_∞ exhibits a non-monotonic dependence on R with a shallow minimum near $R \approx 10$ nm at high VF (15-20 %), where $C_\infty \approx 0.168$ dpa. At smaller radii, curvature-induced coherency strain strengthens interstitial bias ($B > 0$), raising C_∞; at larger radii, geometric sink

dilution ($k^2 \propto \mathrm{VF}/R^2$) weakens overall capture efficiency. The observed optimum therefore marks the intersection of decreasing bias $B \sim 1/R$ (Wei et al., 2024) and diminishing sink strength, establishing the equilibrium between geometry-driven capture and bias-driven asymmetry.

2. Kinetic descriptors: t_x and τ. The temporal metrics—t_{10}, t_{50}, t_{90}—and the effective lifetime τ describe how fast and for how long the system remains kinetically active:

- **Small precipitates** ($R \leq 5$ nm) show extremely short t_{50} ($\sim 10^{-3}$ s) and τ ($\sim 10^{-3}$ s), evidencing bias-driven, short-lived recombination where interstitial absorption dominates.
- **Larger precipitates** ($R \geq 10$ nm) recover more slowly ($t_{50} \approx 10^{-2}$-10^{-1} s, $\tau \sim 10^{-2}$ s) but sustain balanced recombination for longer, leading to lower C_∞.

Thus, t_x and τ trace the kinetic pathway toward equilibrium, while C_∞ defines the endpoint.

3. Normalized recovery metrics: DRE and AE. DRE and AE offer normalized measures of the overall healing capacity and rate efficiency:

- **DRE** parallels C_∞ when C_0 is fixed, serving primarily as a normalized measure for comparing irradiation conditions with differing initial damage.
- **AE** integrates recovery magnitude and rate, peaking in the bias-relaxed regime ($R \approx$7-10 nm, VF 15-20 %), where defect removal is both rapid and sustained. At lower VF (5-10 %), the AE maximum shifts toward $R \approx 15$ nm because reduced sink density delays bias equilibration.

4. Transient measure: $S_{\max}$. The maximum slope $S_{\max}$ characterizes the intensity of early-time defect annihilation. High $S_{\max}$ values in small precipitates ($\sim$ 300 dpa s^{-1}) correspond to bias-dominated, impulsive recombination, whereas larger, high-VF morphologies exhibit smoother transients ($\sim$250 dpa s^{-1}) indicative of bias-relaxed, diffusion-controlled kinetics. Hence, decreasing $S_{\max}$ with R or VF reflects enhanced kinetic stability rather than reduced efficiency.

5. Hierarchy of practical importance: The metrics differ in diagnostic value depending on the irradiation context. Table 5.1 summarizes their relative significance for morphological optimization at 733 K.

Table 5.1: Relative importance of annealing metrics for morphological optimization at 733 K.

Priority	**Metric**	**Physical significance and application**
1 (Primary)	C_∞	Determines residual damage, swelling, and long-term mechanical stab
2 (High)	DRE	Normalized analogue of C_∞; essential when C_0 varies.
3 (High)	AE	Balances rate and completeness; highlights bias-relaxed, fast-healing r
4 (Conditional)	τ, t_{50}, t_{90}	Quantify kinetic endurance; relevant for pulsed or transient irradiatio
5 (Supplementary)	t_{10}	Early onset marker; sensitive to thermal activation.
6 (Diagnostic)	$S_{\max}$	Indicates transient stability and bias relaxation; qualitative compariso

6. Microstructural design framework: Integrating all metrics yields a coherent framework for radiation-tolerant microstructural design:

- **Steady, high-flux operation:** Favor precipitates of $R\approx$10 nm and VF = 15-20 %. These configurations minimize C_∞, maintain sustained recombination ($\tau\sim10^{-2}$ s), and achieve near-zero bias ($B\to0$).
- **Pulsed or intermittent exposure:** Slightly smaller precipitates ($R\approx$5-7 nm) at high VF yield faster early recovery ($t_{50}\sim10^{-3}$-10^{-2} s) between pulses, albeit with marginally higher C_∞.
- **Low-temperature operation:** Diffusion limitations dominate, reducing the effect of bias; optimization should emphasize high VF over radius refinement.

7. Conceptual synthesis. Radiation tolerance does not improve monotonically with decreasing precipitate size. Instead, it emerges from a synergy among three coupled mechanisms:

1. High sink density (short diffusion paths, high recombination probability);
2. Low absorption bias (balanced vacancy-interstitial capture);
3. Moderate kinetic endurance (sustained yet stable healing window).

At 733 K, these factors converge for precipitates of $R \approx 10$ nm and VF = 15-20 %, yielding the lowest residual defect density, maximal AE, and minimal $S_{\max}$. This regime represents a physically balanced, bias-relaxed morphology where geometric capture and interface chemistry act cooperatively to stabilize the microstructure under continuous irradiation.

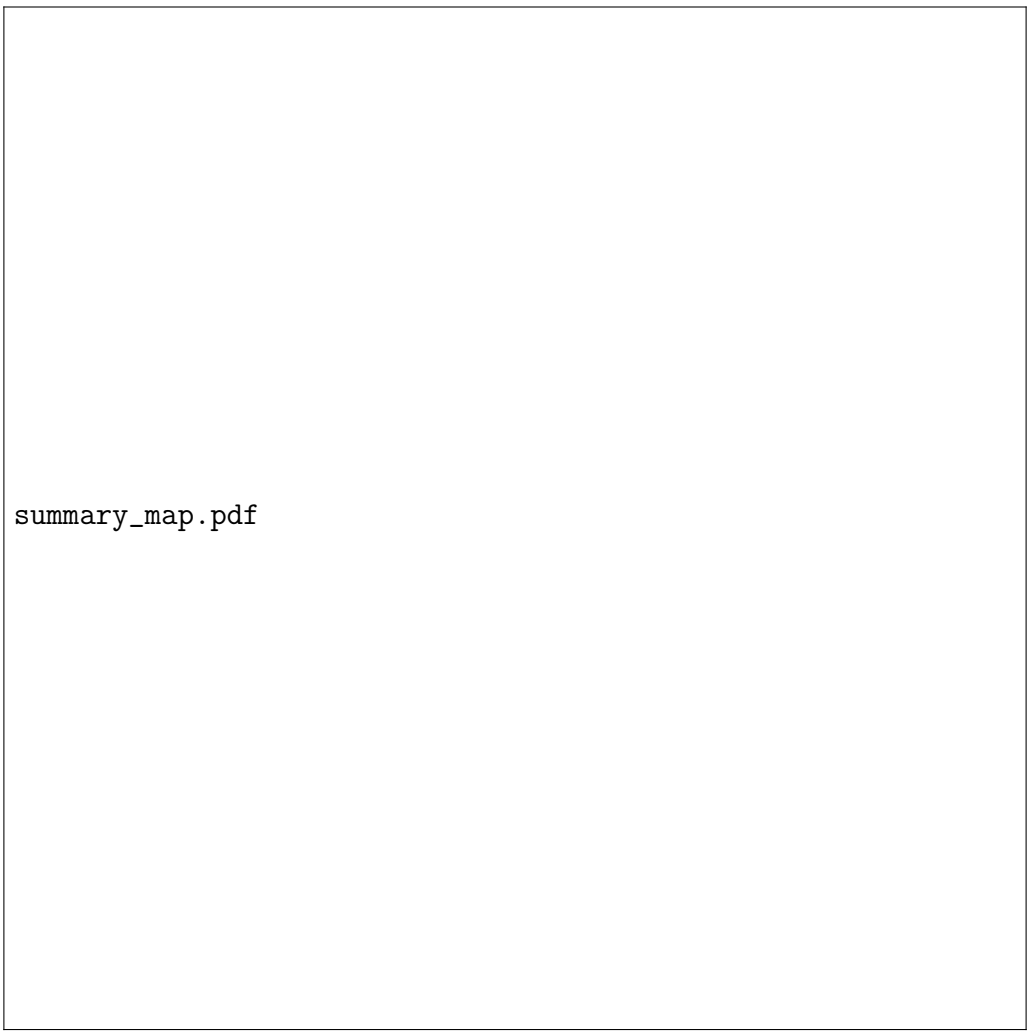

Figure 5.7: Schematic summary of the competing effects of sink density and absorption bias on radiation tolerance. The shaded region indicates the optimal morphology identified by simulations ($R \approx 10$ nm, VF = 15-20 %), corresponding to maximum defect recovery efficiency and minimum residual damage.

5.2 Conclusions

The chemical rate theory (CRT) analysis conducted at 733 K, using primary damage cascades generated by `IM3D` at 1 MeV, establishes a mechanistic framework for linking precipitate morphology to radiation tolerance in Fe-Al-Ni/Fe nanocomposites. By quantifying the evolution of point-defect concentrations as a function of precipitate radius (R)

and volume fraction (VF), the study captures how geometric sink density and interfacial absorption bias jointly govern annealing kinetics and steady-state stability. The principal findings are summarized below:

1. The residual vacancy concentration C_∞ is the most definitive indicator of long-term radiation stability. The minimum value ($C_\infty \approx 0.168\,\text{dpa}$) occurs for precipitates of radius $R{\approx}10\,\text{nm}$ at VF = 15-20 %, representing the morphology that minimizes unrecovered damage under steady irradiation.

2. Increasing volume fraction monotonically reduces C_∞ and accelerates recovery kinetics by increasing the total sink density ($k^2 \propto \text{VF}/R^2$). This demonstrates that total interfacial area is the primary driver of recombination efficiency.

3. The conventional **smaller-is-better** assumption is valid only in the absence of curvature-induced absorption bias. For small precipitates ($R < 5\,\text{nm}$), strong coherency strain enhances interstitial bias ($B > 0$), which accelerates initial recombination but suppresses vacancy absorption, yielding higher residual defect concentrations. Bias relaxation with increasing R ($B{\sim}1/R$; Wei et al., 2024) explains the observed performance optimum near 10 nm.

4. Kinetic parameters (t_{10}, t_{50}, t_{90}, and τ) confirm that smaller precipitates recover defects rapidly but transiently, while larger ones exhibit slower yet sustained recombination over an order of magnitude longer timescale—resulting in lower steady-state damage.

5. Normalized recovery measures (DRE and AE) support the same trend: AE reaches its maximum near $R{\approx}10\,\text{nm}$ and VF = 15-20 %, where curvature-driven bias is largely neutralized and defect capture kinetics remain fast. This configuration optimizes both the magnitude and the rate of recovery.

6. The peak recovery rate $S_{\max}$ decreases systematically with increasing R and VF, marking the transition from impulsive, bias-dominated recombination to smoother, diffusion-controlled kinetics. High $S_{\max}$ in small precipitates corresponds to unstable, transient annihilation that leaves higher residual damage.

7. Radiation tolerance therefore arises from a balance among three coupled mechanisms: (i) geometric sink density governing total capture probability, (ii) curvature-

and strain-induced absorption bias controlling asymmetry between vacancy and interstitial absorption, and (iii) kinetic endurance determining the duration of active recombination. Optimal stability is achieved when these effects are mutually balanced.

Design implications: For structural alloys operating under sustained high-temperature irradiation, the optimal configuration corresponds to **Fe-Al-Ni precipitates of radius** $\sim 10\,$**nm at a volume fraction of 15-20 %**. This morphology provides the best compromise between high sink density and minimal interfacial bias, resulting in the lowest residual defect density and the most stable long-term microstructural evolution. These findings reconcile the classical experimental observation of enhanced tolerance in fine precipitate systems with theoretical predictions of bias-induced asymmetry, offering a mechanistically grounded guideline for designing next-generation radiation-resistant nanostructured alloys.

Bibliography

[1] G. J. Ackland et al. Vacancy migration energy in fe-ni alloys. *Acta Materialia*, 52(14):4287–4295, 2004.

[2] S. V. Divinski et al. Diffusion of vacancies in fe-ni alloys: Prefactor determination. *Journal of Applied Physics*, 103(11):113512, 2008.

[3] C. Domain and C. S. Becquart. Ab initio calculations of defects in Fe and dilute Fe-Cu alloys. *Phys. Rev. B*, 65:024103, 2001.

[4] X. Du, C. Zheng, K. Jin, C. Lu, H. Bei, L. Wang, Y. Zhang, and W.J. Weber. Enhancing radiation tolerance through hierarchical microstructural design. *Nature Materials*, 22:184–193, 2023.

[5] D. Farkas et al. Interstitial defect formation in ni_3al alloys. *Materials Science and Engineering: A*, 338:13–18, 2002.

[6] J. Fu et al. Vacancy migration in bcc fe: A molecular dynamics study. *Acta Materialia*, 56(10):2307–2316, 2008.

[7] Charles Kittel. *Introduction to Solid State Physics*. John Wiley & Sons, Hoboken, NJ, 8th edition, 2005.

[8] Z. Lu et al. Vacancy formation energy in fe-ni alloys. *J. Appl. Phys.*, 109(2):023518, 2011.

[9] M. C. Marinica et al. Interstitial migration energy in ni_3al. *Journal of Nuclear Materials*, 425:21–28, 2012.

[10] H. Mehrer. *Diffusion in Solids: Fundamentals, Methods, Materials, Diffusion-Controlled Processes*. Springer, 2007.

[11] Y. Mishin et al. Vacancy migration in ni$_3$al. *Journal of Materials Science*, 34(12):3107–3114, 1999.

[12] Y. N. Osetsky et al. Interstitial formation and migration energies in fe-ni alloys. *Acta Materialia*, 51(15):4379–4391, 2003.

[13] W. Schaefer. *Vacancy migration in metals and alloys*. Springer-Verlag, Berlin, 1987.

[14] Aram Shirinyan and Yuriy Bilogorodskyy. Effect of radiation-induced vacancy saturation on the first-order phase transformation in nanoparticles: insights from a model. *Beilstein Journal of Nanotechnology*, 15(1):1453–1472, 2024.

[15] R.E. Stoller, M.B. Toloczko, G.S. Was, A.G. Certain, S. Dwaraknath, and F.A. Garner. On the use of srim for computing radiation damage exposure. *Nuclear Instruments and Methods in Physics Research Section B: Beam Interactions with Materials and Atoms*, 310:75–80, 2012.

[16] D. Terentyev et al. Interstitial migration energy in fe-ni alloys. *Journal of Nuclear Materials*, 373:222–226, 2008.

[17] L. Ventelon et al. Interstitial diffusion in fe-ni-al alloys. *Acta Materialia*, 61(16):6079–6086, 2013.

[18] Gary S. Was. *Fundamentals of Radiation Materials Science: Metals and Alloys*. Springer, 2007.

[19] W.J. Weber, Y. Zhang, H. Bei, Y. Gao, C. Lu, and K. Jin. Key factors in radiation tolerance of bcc metals under irradiation. *Progress in Materials Science*, 107:100–180, 2019.

[20] Liuming Wei, Zhe Zhao, Yonggang Li, Qirong Zheng, Chuanguo Zhang, Jingyu Li, Gaofeng Zhao, Bo Da, and Zhi Zeng. Absorption bias: A descriptor for radiation tolerance of polycrystalline bcc metals. *Journal of Nuclear Materials*, 600:155295, 2024.

[21] C. Wolverton et al. Defect properties and diffusion behavior in nial-type alloys: A comprehensive study. *Materials Science and Engineering: A*, 763:138192, 2020.

[22] Y. Yamaguchi et al. Alloying effects on the formation and migration energies of vacancies in ni-based alloys. *Journal of Nuclear Materials*, 216:219–225, 1995.

[23] C. Zheng, K. Jin, H. Bei, W.J. Weber, and Y. Zhang. Radiation-induced defects and their dynamics in materials. *Journal of Nuclear Materials*, 584:153605, 2023.

[24] S.J. Zinkle and B.N. Singh. Microstructure of neutron-irradiated iron before and after deformation. *Journal of Nuclear Materials*, 351:269–284, 2006.